Prediction of anisotropic elastic properties of snow from its microstructure

Citation for published version:
Srivastava, PK, Chandel, C, Mahajan, P & Pankaj, P 2016, 'Prediction of anisotropic elastic properties of snow from its microstructure' Cold Regions Science and Technology, vol. 125, pp. 85-100. DOI: 10.1016/j.coldregions.2016.02.002

Digital Object Identifier (DOI):
10.1016/j.coldregions.2016.02.002

Link:
Link to publication record in Edinburgh Research Explorer

Document Version:
Early version, also known as pre-print

Published In:
Cold Regions Science and Technology

Prediction of anisotropic elastic properties of snow from its microstructure

Praveen K Srivastava[1,2*], Chaman Chandel[1,2], Puneet Mahajan[2] and Pankaj Pankaj[3]

[1]*Snow & Avalanche Study Establishment, Chandigarh, India*
[2] *Applied Mechanics Department, IIT Delhi, New Delhi, India*
[3]*School of Engineering, The University of Edinburgh, Edinburgh, United Kingdom*

ABSTRACT

The elastic properties of snow layers are key determinants for slab avalanche release models. This study investigates the relationships between microstructure and anisotropic elastic properties of snow. We employed micro-finite element (μFE) models built from X-ray micro-computed tomography (μCT) images to compute the effective orthotropic stiffness and compliance tensors for a wide range of snow densities and morphologies. The representativeness of the snow samples for numerical homogenization is rigorously established through the convergence analysis of the computed stiffness tensor and effective isotropic Young's modulus. The microstructure of snow is quantified in terms of ice volume fraction, ice thickness and second rank volume- and surface-based fabric tensors. The isotropic elasticity model based on ice volume fraction could explain 89% of the variability of the stiffness tensor computed by the μFE model with mean relative norm error of 43%. In contrast, the orthotropic elasticity model based on a fabric tensor and the volume fraction raised the adjusted coefficient of determination (r^2_{adj}) to 97% with mean relative norm error of 28%. Overall, the fabric based orthotropic elasticity relationship yielded better results compared to isotropic model with higher r^2_{adj}, lower relative norm errors and smaller dispersion of residuals for the prediction of stiffness tensor components as a whole as well as for the individual elastic constants. We conclude that ice volume fraction in conjunction with fabric descriptors of the snow microstructure can be used to predict the anisotropic elastic properties of snow via the relations established in this study.

Key words: Snow microstructure; Numerical homogenization; Anisotropic elasticity; Fabric tensors; Elasticity-fabric relations

***Corresponding author**

E-mail: praveen.sase@gmail.com

+91-172-2699805, Extn: 238

1. Introduction

Snow is a material with a porous open cellular structure consisting of a complex interconnected network of sintered ice crystals. The layers in a snowpack are subjected to continual structural transformations under the influence of metamorphism and densification processes, resulting in a spectrum of snow microstructure classes (Fierz et al., 2009). The mechanical properties of snow are critical for avalanche hazard assessment (Schweizer et al. 2003) and are intrinsically linked with (a) its microstructure, which refers to the volume fractions and spatial configuration of ice and pore phases, and (b) physical properties of ice. Dry snow slab avalanches are generally released by initiation and rapid propagation of mixed-mode shear-compression fracture in a thin weak layer buried underneath a strong cohesive snow slab (McClung, 1996; Reiweger et al., 2015). The elastic properties of the slab and weak layers are key determinants for slab avalanche release models, which not only influence the transmission of deformation to the weak layer for failure initiation but are also important for fracture propagation in the weak layer (Sigrist and Schweizer, 2007; Habermann et al., 2008; Heierli et al., 2008; Mahajan et al., 2010; Gaume et al., 2015a,b).

The direct measurement of the elastic properties of weak snow classes, such as depth hoar, faceted and surface hoar crystals, from experiments is subject to large errors as sample geometry and loading conditions are often not perfect. Moreover, the pure elastic strain range for snow is very small which makes elastic loading extremely difficult to perform. The structural and mechanical properties of these snow classes also exhibit anisotropy (Reiweger and Schweizer, 2010; Srivastava et al., 2010), which plays an important role in transforming the vertical collapse deformation energy into shear deformation for crack propagation (McClung, 2005). However, physical characterization of the anisotropic stiffness ($\boldsymbol{C}_{ijkl}$) or compliance ($\boldsymbol{S}_{ijkl}$) tensors requires multiple measurements on the same sample that is nearly impossible because of the destructive nature of the tests. Therefore, most of the previous studies (Mellor, 1975, 1977; Frolov and Fedyukin, 1998, Camponovo and Schweizer, 2001; Scapozza and Bartelt, 2003; Sigrist, 2006) assumed snow as an isotropic material and reported quasi-static and dynamic measurements of Young's modulus of relatively well bonded snow in the vertical direction. In these studies, it was found that the Young's modulus of snow is strongly related to its density, however large unexplained variance remained which cannot be attributed solely to different measurements techniques. It is hypothesized that a part of scatter is caused by anisotropy of the snow samples that cannot be accounted for by a scalar quantity such as density.

An alternative is a computational approach using micro-finite element (μFE) methods, where a 3D digitized model of the microstructure is built from high resolution X-ray micro-computed tomography (μCT) images. The homogenized stiffness tensor is then computed over a representative volume element (RVE) of the microstructure for a given set of boundary conditions (Garboczi and Day, 1995). The μFE approach was first used by Schneebeli (2004) to compute the vertical Young's modulus of depth hoar snow. Recently, μFE method was applied on samples from different snow layers to calculate their effective Young's moduli and Poisson's ratios under the assumption of isotropy (Kochle and Schneebeli, 2014). Statistically reconstructed 3D snow microstructure was also used as an input geometry to compute the effective Young's modulus using mesh-free modelling

(Yuan et al., 2010). However, these studies were restricted to computation of effective Young's modulus and Poisson's ratio and the evaluation of the full anisotropic stiffness tensor and its possible relation with snow microstructure was not explored.

The 3D μCT imaging allows characterization of microstructural anisotropy of porous materials by methods such as mean intercept length (MIL) (Whitehouse, 1974), star length distribution (SLD) (Smit et al., 1998) or star volume distribution (SVD) (Cruz-Orive et al., 1992). Applied to snow, these measures can describe the spatial distribution of ice and pore phases with a function that can be approximated by an ellipsoid (Harrigan and Mann, 1984) or by spherical Fourier series (Kanatani, 1984). Both approaches lead to the definition of a positive definite second rank fabric tensor that characterizes the microstructural arrangement and anisotropy in a porous solid. A preliminary study reported significant correlation between MIL fabric measures and Young's moduli of snow (Srivastava et al., 2010) and could explain the anisotropic stiffening under temperature gradient metamorphism. The granular description of structural anisotropy via contact normal tensors (Shertzer and Adams, 2011) looks very appealing, however grain segmentation and identification of grain contacts in 3D μCT images of snow microstructure is not trivial. Recently, Hagenmuller et al. (2014a) introduced a new microstructural parameter, the minimum cut density, which describes the reduced thickness of the ice matrix at bonds and showed good correlation with anisotropic Young's modulus of faceted snow. However, its relationship with all the components of the stiffness tensor is yet to be explored.

The mathematical basis for relationship between a second rank fabric tensor characterizing microstructure and the fourth rank elasticity tensor was first proposed by Cowin (1985). Following this approach, Zysset et al. (1998) developed an orthotropic elasticity model which also ensured the positive definiteness of the elasticity tensor a priori and can be reduced into (at least) a cubic symmetry model when the eigenvalues of the fabric tensor coincide. The generalized Zysset-Curnier orthotropic elasticity model (Zysset et al., 1998) consisted of five material constants besides fabric tensor and volume fraction. An extensive review by Zysset (2003) listed the formulations of existing theoretical morphology-elasticity models and compared them by applying to a common data set of trabecular bone and idealized open and closed cell 3D structures. The fabric tensor based morphology-elasticity models are very appealing as they provide an alternative to the much more computationally expensive μFE methods. In absence of μCT-images, polar distribution of mean intercept length on 2D vertical snow sections can be used to obtain a measure of structural anisotropy. Alternatively, Kuo et al. (1998) approach could be used to approximate the MIL fabric tensor in 3D from stereological measurements on three mutually-perpendicular planar sections of snow samples.

The main objective of this study was to investigate if elastic properties of snow can be reliably predicted on the basis of either ice volume fraction alone or in conjunction with fabric tensors. We employed voxel based μFE simulations on μCT images to compute the homogenized stiffness tensors for a wide range of snow densities. The microstructural anisotropy was characterized using surface- and volume-based fabric measures. The μFE and fabric results were analysed statistically against isotropic and orthotropic morphology-elasticity relationships. Our findings confirm that ice volume fraction along with fabric are the best determinants of the anisotropic elastic properties of snow using μCT imaging.

2. Materials and Methods

2.1 Snow Samples

The numerical analyses were performed on a heterogeneous collection of 25 snow samples. These samples were either obtained via field sampling or prepared using controlled cold-lab experiments. A description of the samples, including their classification according to the International Classification for Seasonal Snow on the Ground (Fierz et al., 2009), is given in **Table 1**. The analyzed samples span most of the seasonal snow classes (**Figure 1)**: 2 samples of Precipitation Particles (PP), 1 of Decomposing and Fragmented precipitation particles (DF), 9 of Rounded Grains (RG), 8 of Faceted Crystals (FC) and 5 of Depth Hoar (DH). Seven samples (HF1 – HF7) were prepared from kinetic metamorphism experiments where the snow samples evolved under a fixed temperature gradient of 96 K m^{-1} (Srivastava et al., 2010). These samples correspond to various stages of transformations into facetted crystals and depth hoar. Four of the RG snow samples (ET1, T1, T2 and T3) were prepared under isothermal conditions at 264 K after sieving. Another RG sample (MTS1) was taken from the data of Chandel et al. (2014). The remaining samples comprising various snow classes were directly collected from Patsio (32 45’N, 77 16’E; 3800 m a.s.l.) and Dhundhi (32 21’N, 77 7’E; 3050 m a.s.l) field research stations in the Indian Himalayas. All the samples were scanned non-destructively with a Skyscan 1172 (Bruker, Belgium) X-ray micro-computed tomography system at resolutions ranging between 4.97 μm and 8.56 μm. The resolutions of the images were further reduced by a factor of three or four to allow reasonable computational times. The grayscale images were filtered with a 3^3 median filter and segmented into ice and pore phases. The resulting cubic volumes of side-length ranging from 5.96 mm to 9.55 mm were used for the microstructure analysis and numerical computation of elastic properties.

2.2 Microstructure Parameters and Construction of Fabric Tensors

The microstructure was characterized in terms of ice volume fraction (υ_s), ice thickness (h_{ice}), pore thickness (h_{pore}), and volume- and surface-based fabric tensors. υ_s was calculated using the hexahedral marching cube volume model (Lorensen and Cline, 1987). h_{ice} and h_{pore} defined as the mean diameter of ice structures and pores in snow respectively, were obtained using the distance transform of the ice matrix and pores (Hildebrand and Ruegsegger, 1997). The density of snow (ρ_s) was calculated by multiplying υ_s with density of ice ($\rho_{\text{ice}} = 917$ kg m^{-3}).

Fabric tensors can provide quantitative characterization of both anisotropy and orientation of the material phase of interest. In this study we used second rank MIL, SLD and SVD fabric tensors to characterize the three planes of orthotropic symmetry and degree of microstructural anisotropy. The MIL is defined as the mean distance between two solid/pore interfaces in a given direction. The distribution of the MIL at a point in 3D space forms an ellipsoid, and provides a second rank fabric tensor **H** (Harrigan and Mann, 1984). The MIL fabric tensor is defined as the inverse square root of **H**. The SLD is constructed by placing a sequence of points in the ice phase and measuring the lengths of lines emanating from the points until they encounter a solid/pore interface (Smit et al., 1998). The SVD is also constructed by placing a sequence of points in the ice phase, but instead of lines infinitesimal cones are used (Cruz-Orive et al., 1992). Because MIL traverses multiple phase boundaries, they reflect anisotropy of the configuration of the pore/solid interface, while the star analyses account for the directional configuration of the ice phase. All the directional measurements were carried out using QUANT3D (Ketcham and Ryan, 2004).

In general, the positive definite second rank fabric tensor $\mathbf{M}$ can be expressed as (Cowin, 1985; Zysset, 2003):

$$\mathbf{M} = \sum_{i=1}^{3} m_i \mathbf{M_i} = \sum_{i=1}^{3} m_i (\mathbf{m_i} \otimes \mathbf{m_i}), m_3 \leq m_2 \leq m_1 \tag{1}$$

where m_i are the strictly positive eigenvalues and $\mathbf{m_i}$ the normalized eigenvectors. Since the fabric tensors defined by MIL, SLD and SVD have different physical units, they were normalized by their trace, $\mathrm{tr}(\mathbf{M}) = \alpha > 0$.

The relationship among fabric tensor eigenvalues may be thought of as representing a continuum of fabric shapes, varying between three end members: spheres ($m_1 \approx m_2 \approx m_3$), discs ($m_1 \approx m_2 \gg m_3$), and rods ($m_1 \gg m_2 \approx m_3$). Benn (1994) defined an isotropy index (I) and an elongation index (EI) to describe the fabric shape as,

$$I = \frac{m_3}{m_1}; \quad EI = 1 - \left(\frac{m_2}{m_1}\right); \tag{2}$$

Using these indices, it is possible to describe and compare snow fabric characteristics across different snow types.

2.3 μFE computations of elastic properties

The linear elastic properties of snow were computed from μCT data using a voxel-based FE programme (Bohn and Garboczi, 2003). μFE models of segmented cubical volumes of snow were created by converting image voxels into homogeneous linear hexahedral elements. For ice, linear elastic and isotropic properties were specified with a Young's modulus of 9.5 GPa and Poisson's ratio of 0.3 (Sanderson, 1988). The homogenized elastic properties of μFE models were evaluated by performing FE simulations of six independent load cases (three compressive and three shear tests) under periodic boundary conditions. The loading in each case is in the form of the imposed unit macroscopic strains,

$$\begin{Bmatrix} e_{11} \\ e_{22} \\ e_{33} \\ e_{23} \\ e_{13} \\ e_{12} \end{Bmatrix} = \begin{Bmatrix} 1 \\ 0 \\ 0 \\ 0 \\ 0 \\ 0 \end{Bmatrix}, \begin{Bmatrix} e_{11} \\ e_{22} \\ e_{33} \\ e_{23} \\ e_{13} \\ e_{12} \end{Bmatrix} = \begin{Bmatrix} 0 \\ 1 \\ 0 \\ 0 \\ 0 \\ 0 \end{Bmatrix}, \begin{Bmatrix} e_{11} \\ e_{22} \\ e_{33} \\ e_{23} \\ e_{13} \\ e_{12} \end{Bmatrix} = \begin{Bmatrix} 0 \\ 0 \\ 1 \\ 0 \\ 0 \\ 0 \end{Bmatrix} \tag{3a}$$

$$\begin{Bmatrix} e_{11} \\ e_{22} \\ e_{33} \\ e_{23} \\ e_{13} \\ e_{12} \end{Bmatrix} = \begin{Bmatrix} 0 \\ 0 \\ 0 \\ 1 \\ 0 \\ 0 \end{Bmatrix}, \begin{Bmatrix} e_{11} \\ e_{22} \\ e_{33} \\ e_{23} \\ e_{13} \\ e_{12} \end{Bmatrix} = \begin{Bmatrix} 0 \\ 0 \\ 0 \\ 0 \\ 1 \\ 0 \end{Bmatrix}, \begin{Bmatrix} e_{11} \\ e_{22} \\ e_{33} \\ e_{23} \\ e_{13} \\ e_{12} \end{Bmatrix} = \begin{Bmatrix} 0 \\ 0 \\ 0 \\ 0 \\ 0 \\ 1 \end{Bmatrix} \tag{3b}$$

The full homogenized stiffness tensor of each snow cube was computed by means of stress and strain averages of the FE analysis results. In its most general form, the 6×6 matrix representation of anisotropic stiffness tensor, defined relative to the image coordinate system, involves 21 independent elastic coefficients and is given by

$$[C_{FE_{aniso}}] = \begin{bmatrix} c_{11} & c_{12} & c_{13} & \delta_{14} & \delta_{15} & \delta_{16} \\ c_{12} & c_{22} & c_{23} & \delta_{24} & \delta_{25} & \delta_{26} \\ c_{13} & c_{23} & c_{33} & \delta_{34} & \delta_{35} & \delta_{36} \\ \delta_{14} & \delta_{24} & \delta_{34} & c_{44} & \delta_{45} & \delta_{46} \\ \delta_{15} & \delta_{25} & \delta_{35} & \delta_{45} & c_{55} & \delta_{56} \\ \delta_{16} & \delta_{26} & \delta_{36} & \delta_{46} & \delta_{56} & c_{66} \end{bmatrix} \quad (4)$$

If planes of elastic symmetry exist, some of these coefficients are interdependent or zero when measured in a coordinate system aligned with the normals to the symmetry planes (Cowin and Mehrabadi, 1987). In the case of orthotropy, off-diagonal elements, denoted δ_{ij}, are zero when the three loading directions parallel the normal vectors of the three planes of orthotropic symmetry and the number of independent elastic constants are reduced to 9. For materials that do not have pure orthotropic symmetries, values of δ_{ij}, are non-zero but small relative to the c_{ij}, terms. A numerical optimization procedure was then used to find the coordinate transformation that minimizes an orthotropy objective function defined as (Rietbergen et al., 1996)

$$Obj = \frac{\sum_{i,j} \delta_{ij}^2}{\sum_{i,j} c_{ij}^2}, i, j = 1, \dots, 6 \quad (5)$$

The non-orthotropic entries of the transformed stiffness tensor, $\boldsymbol{C}_{FE_{aniso}}$, were then set to zero to obtain the best orthotropic representation of the stiffness tensor, $\boldsymbol{C}_{FE_{ortho}}$. The relative norm error (NE^{ortho}) caused by forcing orthotropic symmetry is quantified by,

$$NE^{ortho} = \frac{\left\| \boldsymbol{C}_{FE_{aniso}} - \boldsymbol{C}_{FE_{ortho}} \right\|}{\left\| \boldsymbol{C}_{FE_{aniso}} \right\|} \quad (6)$$

The matrix form of corresponding orthotropic compliance tensor $\boldsymbol{S}_{FE_{ortho}}$ is given by,

$$[\boldsymbol{S}_{FE_{ortho}}] = [\boldsymbol{C}_{FE_{ortho}}]^{-1} = \begin{bmatrix} \frac{1}{E_1} & -\frac{\nu_{21}}{E_2} & -\frac{\nu_{31}}{E_3} & 0 & 0 & 0 \\ -\frac{\nu_{12}}{E_1} & \frac{1}{E_2} & -\frac{\nu_{32}}{E_3} & 0 & 0 & 0 \\ -\frac{\nu_{13}}{E_1} & -\frac{\nu_{23}}{E_2} & \frac{1}{E_3} & 0 & 0 & 0 \\ 0 & 0 & 0 & \frac{1}{2G_{23}} & 0 & 0 \\ 0 & 0 & 0 & 0 & \frac{1}{2G_{31}} & 0 \\ 0 & 0 & 0 & 0 & 0 & \frac{1}{2G_{12}} \end{bmatrix} \quad (7)$$

where E_i, G_{ij} and ν_{ij} are the engineering constants.

The effective isotropic Young's modulus (E_{eff}) and Poisson's ratio (ν_{eff}) of each snow cube was estimated from the bounds on effective isotropic bulk (k_{eff}) and shear (G_{eff}) moduli of an orthotropic material (Cowin et al., 1999; Yoon et al.,2002),

$$k_R \leq k_{eff} \leq k_V, \quad G_R \leq G_{eff} \leq G_V \quad (8)$$

where the subscript R (V) stands for the Reuss (Voigt) bounds on k_{eff} and G_{eff}. The Voigt and Reuss bounds can be determined from the components of the matrix representation of $\boldsymbol{C}_{FE_{ortho}}$ and its corresponding compliance tensor $\boldsymbol{S}_{FE_{ortho}}$ (Hill, 1952),

$$k_V = \frac{1}{9}(c_{11} + c_{22} + c_{33}) + \frac{2}{9}(c_{12} + c_{23} + c_{31})$$

$$k_R = \frac{1}{(s_{11} + s_{22} + s_{33}) + 2(s_{12} + s_{23} + s_{31})} \quad (9)$$

and

$$G_V = \frac{1}{15}(c_{11} + c_{22} + c_{33} - c_{12} - c_{23} - c_{31}) + \frac{1}{5}(c_{44} + c_{55} + c_{66})$$

$$G_R = \frac{1}{(4/15)(s_{11} + s_{22} + s_{33} - s_{12} - s_{23} - s_{31}) + (1/5)(s_{44} + s_{55} + s_{66})} \quad (10)$$

The upper Voigt and lower Reuss bounds on k_{eff} and $G_{eff},$ computed on the full image volumes, were found to be very close for the snow samples considered (**Figure 2**). Consequently, the values of k_{eff} and G_{eff} are simply computed as the average of these bounds and converted into equivalent E_{eff} and ν_{eff} as,

$$E_{ff} = \frac{9K_{eff}G_{eff}}{3K_{eff} + G_{eff}}, \nu_{eff} = \frac{3K_{eff} - 2G_{eff}}{2(3K_{eff} + G_{eff})} \quad (11)$$

2.4 Representative Volume Element (RVE)

Criteria for the RVE are often linked to continuum modeling assumptions (Nemat-Nasser and Hori, 1998), convergence of a given property (Swaminathan et al., 2006), or statistical representation of specific microstructural features (Kanit et al., 2003, Niezgoda et al., 2010). In homogenization problems, the RVE essentially refers to the smallest volume element of the microstructure that is statistically representative of the porous material as a whole while effectively smoothing out the local heterogeneities in such a way that the homogenized macroscopic properties are captured to a desired accuracy (Swaminathan et al., 2006; Niezgoda et al., 2010). The success of RVE-based homogenization critically relies on satisfaction of the assumption of scale decoupling (Nemat-Nasser and Hori, 1998) i.e. $\delta := l_{RVE}/l_{micro} \gg 1$, where l_{micro} is the length scale of the individual microstructure heterogeneities (e.g. grains, pores) and l_{RVE} is the linear size of RVE. We investigated the size of the RVE by performing numerical computations on concentric cubic snow volumes of increasing sizes. The smallest volume for which the E_{eff} as well as the norm of the effective orthotropic stiffness tensor, $\|\boldsymbol{C}_{FE_{ortho}}\|$, converged (at least locally) to that for the entire microstructure within a specified tolerance of 20% was taken as the RVE.

The convergence based RVE criteria lacks explicit connection between inherent microstructural variability in a material and the variability in elastic properties. In order to investigate the statistical variability, the total volume of each of the snow samples (300^3 voxel^3) was partitioned into three sets of cubical sub-volumes, i.e. (i) set of 64 cubes with edge length (*L*)=75 voxel, (ii) set of 27 cubes with *L*=100 voxel, and (iii) set of 8 cubes with *L*=150 voxel (**Figure 3**). Depending on the resolution of individual snow images, the cube edge lengths of 150 voxel, 100 voxel and 75 voxel translated into physical edge lengths of 2.6-4.8 mm, 1.7-3.2 mm and 1.3-2.4 mm respectively. The stiffness tensors for all the sub-volumes of different sets were computed for investigating the effect of sub-volume sizes on the relative variability of E_{eff} and υ_s.

2.5 Isotropic and Orthotropic Morphology-Elasticity Models

Based on the power law relations between elastic moduli and solid volume fraction, an isotropic (ISO) model that relates compliance (**S**) and stiffness (**C**) tensors to ice volume fraction (υ_s) can be expressed as (Zysset, 2003),

$$\mathbf{S}(\upsilon_s) = -\frac{\nu_0}{E_0\upsilon_s^k}\mathbf{I}\otimes\mathbf{I} + \frac{\nu_0 + 1}{E_0\upsilon_s^k}\mathbf{I}\underline{\overline{\otimes}}\mathbf{I} \tag{12}$$

$$\mathbf{C}(\upsilon_s) = \lambda_0\upsilon_s^k\,\mathbf{I}\otimes\mathbf{I} + 2G_0\upsilon_s^k\,\mathbf{I}\underline{\overline{\otimes}}\mathbf{I} \tag{13}$$

where $\{E_0, \nu_0, \mathrm{k}\}$ and $\{\lambda_0, G_0, \mathrm{k}\}$ are alternative but equivalent sets of ISO model constants. In particular, for a nonporous solid (i.e. $\upsilon_s = 1$), the model constants λ_0 and G_0 are interpreted as Lamé constants, E_0 the elastic modulus and ν_0 the Poisson's ratio. The exponent k characterizes the power law dependence on the ice volume fraction. **I** is the second rank identity tensor and the double tensorial products $\mathbf{K} = \mathbf{A}\otimes\mathbf{B}$ and $\mathbf{K} = \mathbf{A}\underline{\overline{\otimes}}\mathbf{B}$ are equivalent to $K_{ijkl} = A_{ij}B_{kl}$ and $K_{ijkl} = \frac{1}{2}\left(A_{ik}B_{jl} + A_{il}B_{jk}\right)$, respectively.

The Zysset-Curnier (ZC) fabric-elasticity model (Zysset, 2003) predicts positive definite fourth rank orthotropic compliance and stiffness tensors using volume fraction in the range [0, 1] and an arbitrary second rank fabric tensor **M** as,

$$\mathbf{S}(\upsilon_s, \mathbf{M}) = \sum_{i=1}^{3}\frac{1}{E_0\upsilon_s^k m_i^{2l}}(\mathbf{M_i}\otimes\mathbf{M_i}) - \sum_{i,j=1;i\neq j}^{3}\frac{\nu_0}{E_0\upsilon_s^k m_i^l m_j^l}\left(\mathbf{M_i}\otimes\mathbf{M_j}\right) + \sum_{i,j=1;i\neq j}^{3}\frac{1}{2G_0\upsilon_s^k m_i^l m_j^l}\left(\mathbf{M_i}\underline{\overline{\otimes}}\mathbf{M_j}\right) \tag{14}$$

$$\mathbf{C}(\upsilon_s, \mathbf{M}) = \sum_{i=1}^{3}(\lambda_0 + 2G_0)\upsilon_s^k m_i^{2l}(\mathbf{M_i}\otimes\mathbf{M_i}) + \sum_{i,j=1;i\neq j}^{3}\lambda_0'\upsilon_s^k m_i^l m_j^l\left(\mathbf{M_i}\otimes\mathbf{M_j}\right) + \sum_{i,j=1;i\neq j}^{3}2G_0\upsilon_s^k m_i^l m_j^l\left(\mathbf{M_i}\underline{\overline{\otimes}}\mathbf{M_j}\right) \tag{15}$$

where $\{E_0, \nu_0, G_0, k, l\}$ and $\{\lambda_0, \lambda_0', G_0, k, l\}$ are alternative but equivalent sets of ZC model constants. The ZC model reduces into ISO model if $\mathbf{M} = \mathbf{I}$ and the following relation holds (Zysset, 2003),

$$G_0 = \frac{E_0}{2(1+\nu_0)} \quad or\ \lambda_0 = \lambda_0' \tag{16}$$

The choice of $\mathrm{tr}(\mathbf{M}) = 3$ ensures that the model constants E_0, G_0 and ν_0 can be interpreted as elastic modulus, shear modulus, and Poisson's ratio of a solid (no porosity) $\upsilon_s = 1$ and (at least) cubic $\mathbf{M} = \mathbf{I}$ **(** $\mathrm{m}_i = 1$**)** material (Zysset et al., 1998; Zysset, 2003). Additionally, if the relation $G_0 = \frac{E_0}{2(1+\nu_0)}$ $or\ \lambda_0 = \lambda_0'$ also holds, then the ZC model constants can be interpreted as the elastic properties of an extrapolated isotropic material with volume fraction $\upsilon_s = 1$.

The parameters of ISO and ZC models were fitted to the μFE and fabric results by constructing multiple linear regression equations of the form,

$$\boldsymbol{y} = \mathbf{Xc} + \mathbf{e} \tag{17}$$

where vector $\boldsymbol{y}$ is a *12n* vector consisting of log-transformed 12 non-zero components of the orthotropic compliance or stiffness tensor for *n* samples, **X** is the *12n* × *p* matrix containing the ice volume fraction and fabric data, **c** is a vector of the *p* model constants and vector **e** contains the residuals. The linear system of equations was then solved for **c** by minimizing the sum of squared residuals leading to,

$$\mathbf{c} = (\mathbf{X}^{\mathbf{T}}\mathbf{X})^{-\mathbf{1}}\mathbf{X}^{\mathbf{T}}\mathbf{y} \tag{18}$$

The ZC model was evaluated using each of the three fabric tensors (MIL, SLD and SVD) to investigate if volume based fabric measure provides a closer fit to compliance and stiffness tensors than surface based fabric descriptors. The model fits were evaluated by analysing both magnitude of the residuals and the adjusted coefficient of determination (r_{adj}^2). Further, the model norm error (NE^{model}) describing the relative variation between the predicted and μFE calculated elasticity tensor was quantified as,

$$NE^{model} = \frac{\left\|\boldsymbol{S}_{FE_{ortho}} - \boldsymbol{S}_{model}\right\|}{\left\|\boldsymbol{S}_{FE_{ortho}}\right\|} \ \ or \ \frac{\left\|\boldsymbol{C}_{FE_{ortho}} - \boldsymbol{C}_{model}\right\|}{\left\|\boldsymbol{C}_{FE_{ortho}}\right\|} \tag{19}$$

3. Results and Discussion

3.1 Representative volume element considerations

The convergence of υ_s, E_{eff}, and $\left\|\boldsymbol{C}_{FE_{ortho}}\right\|$ with increasing cubic volume size is shown in **Figure 4**. Volume fraction υ_s was found to converge in the volume range [1.5^3, 2.5^3] mm^3 within the tolerance of 20% for all the snow samples. The values of E_{eff} and $\left\|\boldsymbol{C}_{FE_{ortho}}\right\|$ can also be observed to progressively converge to that for the entire microstructure. The critical RVE can be well approximated to be in the volume range [4.0^3-6.5^3] mm^3 for all samples except M1 and M2. For these low density (97-130 kgm^{-3}) PP snow samples, the RVE appears to be larger than the available scanned volume. As a comparison, the RVE for a μFE based constrained uniaxial simulations of the effective Young's modulus of low density snow ($\rho_s < 300$ kg m^{-3}) was around 6.5^3 mm^3 (Kochle and Schneebeli, 2014). The RVE for the effective thermal conductivity of snow (Calonne et al., 2011) was reported in the range of [2.5^3-5.5^3] mm^3. Additionally, RVE sizes for the minimum cut-density, a parameter which showed excellent correlation with Young' modulus of snow, were also determined in the range of [3^3-6^3] mm^3 (Hagenmuller et al., 2014a). The RVE estimates with respect to the stiffness tensor of snow obtained in this study are consistent with previously reported estimates for other properties.

Any volume larger than the minimum RVE size can be regarded as representative and thus maximum available image volume for each of the snow samples fulfills the RVE criteria with respect to the effective stiffness tensor except for samples M1 and M2. Even if an RVE cannot be realized due to physical size constraints for M1 and M2, the stiffness tensors corresponding to maximum available volumes can be still used to describe apparent properties (Huet, 1990). Approximating l_{micro} by h_{ice} , the values of $\delta := L/h_{ice}$ corresponding to the full image volume of the samples were found to be in the range 17 to 75. Alternatively taking $l_{micro} \cong h_{pore}$, $\delta' := L/h_{pore}$ ranges from 12 to 50. The relatively high values of δ (73 and 51) for samples M1 and M2 seems to fulfil the condition $\delta \gg 1$, however the corresponding values of δ'(16 and 12) appears to be too low to satisfy $\delta' \gg 1$. It should be noted that to satisfy the assumption of scale decoupling, the two conditions $\delta \gg 1$ and $\delta' \gg 1$ should be separately fulfilled. Previous studies have employed $\delta := l_{RVE}/l_{micro}$ in the range between 10 and 100 for elastic response of heterogeneous materials (Xu and Chen, 2009; Ostoja-Strzewski, 2008).

The structural inhomogeneity within individual image volumes was analysed in terms of the statistical uncertainties of the μFE results in three different sets of cubical sub-volumes with edge lengths of 75 voxel, 100 voxel and 150 voxels respectively. **Figure 5** shows the variation of mean E_{eff} versus mean υ_s for the corresponding sub-volumes. The horizontal and vertical error bars represent ±1 standard deviation of υ_s and E_{eff} respectively. The value of E_{eff} for the entire microstructure (300 voxel cube) for all samples is also shown for reference. The variability of both E_{eff} and υ_s increases with decreasing sub-volume sizes, which is to be expected as the statistical fluctuations between individual sub-volumes are expected to be larger as the volumes become smaller. The mean E_{eff} for cubic volumes of 150^3 voxels or $[2.6^3\text{-}4.8^3]$ mm^3 appear to be consistent with the data for the largest available volumes (**Figure 5c**). However, the results with smaller volumes of 100^3 voxels and 75^3 voxels show a bias in mean $E_{eff,}$ particularly for $\upsilon_s <$ 0.30 (**Figure 5a and 5b**). This is attributed to the larger relative microstructural heterogeneity in the smaller volumes of low density snow as indicated by the increased standard deviations of υ_s for smaller sub-volumes.

Figure 5d shows a nearly perfect linear relationship between the coefficient of variation (CV) of ice volume fraction, $(\upsilon_s)_{CV}$, and that of effective isotropic Young's modulus $\left(E_{eff}\right)_{CV}$. This linear scaling relation between the relative variability of a measure of microstructure and the relative variability of effective property, $\left(E_{eff}\right)_{CV} = \gamma(\upsilon_s)_{CV}$, holds for an ensemble of snow classes spanning a wide range of densities (97 - 533 kgm^{-3}). F**igure 5d** includes a 95% confidence limit of the linear fit, γ = 4.56 (4.41-4.70) when data for all the smaller sub-volumes are used for regression which can be a valuable tool for exploring an alternate volume element description that is better linked to the material parameters of microstructure and elastic properties. A basic microstructural volume element ($RVE_{structure}$) size for υ_s can be defined which scale with a minimal set of relevant microstructural features, such as (υ_s, l_{micro}). The RVE for elastic properties ($RVE_{elastic}$) is then directly linked to $RVE_{structure}$ by the linear scaling relation between $(\upsilon_s)_{CV}$ and $\left(E_{eff}\right)_{CV}$ which provides adequate information to a priori decide about the $RVE_{elastic}$ with acceptable level of microstructural and property uncertainties.

3.2 Effective Isotropic Young's modulus and Poisson ratio

Figure 6a shows the plot of E_{eff} versus density for comparison with previously published experimental and numerical results. The plot includes E_{eff} computed over the entire microstructure (300^3 voxels or [5.96^3-9.55^3] mm^3) as well as that obtained over an ensemble of 8 sub-volumes (150^3 voxels or [2.6^3-4.8^3] mm^3) for each snow sample. Interestingly, choosing smaller but representative sub-volumes provides an ensemble of independent samples from a single snow image and allowed us to explore effective elastic properties variation across a range of snow densities. The data indicate that, overall, simulated E_{eff} values compare quite well with the previous dynamic measurements (region A and curve B, Shapiro et al., 1997) and follow closely the exponential fits from µFE based simulations (curve D, Kochle and Schneebeli, 2014). The results from low strain-rate and creep tests (region C, Shapiro et al., 1997), quasi-static compression experiments (Curve E, Scapozza and Bartelt, 2003), and dynamic measurements at 100 Hz (Curve F, Sigrist 2006) are significantly lower compared to our results. It is interesting to note that the strain rate corresponding to frequency of 100 Hz in Sigrist (2006) is 2.7 x 10^{-2} s^{-1}, which may not be high enough to be completely in the elastic range (McClung, 2007). The flexural vibration data (Mellor, 1975) at density 400 kg m^{-3} are at least 50% higher than values provided by

Sigrist (2006). McClung (2007) pointed out that for snow and ice, a clear distinction has to be made between the “elastic modulus" which can be measured only at very high frequencies and the “effective modulus” at lower frequencies or from static creep and low strain rate tests. While the simulated E_{eff} represents the elastic moduli independent of frequency and depends primarily on snow density; the effective moduli reported in Sigrist (2006) represent a combination of truly elastic (recoverable) and viscoelastic response that depend on loading rate or frequency for a given density. Note, however, that below the density of 200 kg m^{-3}, the computed E_{eff} shows good match with Sigrist (2006) parameterization.

The empirical parameterizations of E_{eff} with density by power (Frolov and Fedyukin, 1998; Sigrist, 2006) or exponential (Scapozza and Bartelt, 2003; Kochle and Schneebeli, 2014) relationships might provide a convenient way of summarizing the data for narrow ranges of density but lack the vigorous connection with microstructure which is required to explain the anisotropic elastic properties of snow.

The effective isotropic Poisson's ratio showed no clear trend with density **(Figure 6b)**. Similar to E_{eff}, the ν_{eff} values computed over sub-volumes of size 150^3 voxels were consistent with those obtained over the entire image volume, at least for density > 200 kg m^{-3}. Among the snow classes, RG shows almost a constant value of 0.191± 0.008 over the density range of 200-580 kg m^{-3}. The largest scatter was found for PP and DF particles with mean value of 0.132±0.053, while faceted (FC) and depth hoar (DH) snow show intermediate scatter with mean value of 0.17±0.02. Our estimates of ν_{eff} are lower than the dynamic measurements of Poisson's ratio for density > 400 kgm^{-3} (region D, Smith, 1969), but comparable to the values reported by Kochle and Schneebeli (2014).

3.3 Fabric Tensors and Orthotropic Elastic Constants

The normalized eigenvalues ($m_{i:}\, m_3 \leq m_2 \leq m_1$) of SVD, SLD and MIL fabric tensors ($\mathrm{tr}(\mathbf{M}) = 1$) are summarized in **Table 2**. The computed orthotropic elastic parameters (E_i, G_{ij}, ν_{ij}) are given in **Table 3**. The tabulated values correspond to the maximum image volume available for each sample. The mean norm error (NE^{ortho}) associated with orthotropic representations ($\boldsymbol{C}_{FE_{ortho}}$) of the anisotropic stiffness tensors ($\boldsymbol{C}_{FE_{aniso}}$) was approximately 5.5%. In order to explore the relationship between m_i and mechanical parameters, normalized Young's moduli (E_{Ni}: E_{N1}, E_{N2}, E_{N3}) and normalized shear moduli (G_{Nij}: $G_{N12}, G_{N13}, G_{N23}$)were calculated such that, $E_{N1} + E_{N2} + E_{N3} = 1$ and $G_{N12} + G_{N13} + G_{N23} = 1$. The normalized quantities fundamentally reflect the anisotropic mechanical properties due solely to the microstructural anisotropy as represented by its fabric.

The concept of fabric anisotropy describes the non-random distribution of material in 3D (Odgaard et al., 1997). **Figure 7a-c** shows bivariate plots of elongation index (EI) vs. isotropic index (I) for SVD, SLD and MIL fabric tensors respectively. EI used in combination with I, provides a specific characterization of the material distribution in 3D. The value of $I = 1$ indicates a full isotropic fabric with material equally distributed in all directions, while I=0 is indicative of more anisotropic structure. Similarly $EI = 1$ indicates an isotropic fabric while EI approaching zero means a rod like elongated fabric. There are clear snow type dependent effects, most notably that the majority of FC and DH snow samples (except G2 and G3) seemed to appear in a cluster separate from the other samples from RG and PP+DF snow types**. Figure 8** depicts the ternary shape diagram (Benn, 1994) of fabric anisotropy corresponding to SVD measure. A completely isotropic fabric appears at the apex, an anisotropic structure with an elongated unidirectional fabric would make an appearance at the right corner, and a planar anisotropic fabric at the left corner. Although there is overlap, PP, DF and RG snow fabric tends to be more isotropic while FC and DH snow tend to be more anisotropic. On closer examination of G2 and G3 sample images, it emerged that these were not homogeneous with respect to snow type and seemed to be a combination of round grain and highly faceted snow types. Additionally, FC and DH snow exhibit much stronger fabric anisotropy compared to RG and PP+DF snow.

Figure 7d depicts the bivariate plot between mechanical elongation (EI_{Mech}) and isotropy (I_{Mech}) indices which are defined as, $I_{Mech} = E_{N3}/E_{N1}$ and $EI_{Mech} = 1 - (E_{N2}/E_{N1})$. Concerning the mechanical anisotropy, Figure 7d presents a more complicated picture with larger overlap between the FC/DH and PP/DF/RG clusters. This might be due to the low-scale randomness of the snow microstructure in the μFE models which is lost by the stereological averaging process involved in the computation of second rank fabric tensors. Additionally, we found no clear trend between sample anisotropy indices and ice volume fraction (**Figure 9**).

Figure 10 shows typical representation surfaces of orthotropic stiffness tensors obtained via the numerical μFE optimization procedure for PP, RG, FC and DH snow classes. The corresponding ellipsoidal surfaces of SVD and MIL fabric measures in the image coordinate system (**Figure 10)** suggest that both volume and surface based fabric measures come very close to the mechanical main directions. The SVD fabric measure is appearing as a better descriptor for characterizing the anisotropy in elastic properties. **Figure 11a-c** shows the plots between E_{Ni} and m_i for the three fabric measures. The Pearson correlation coefficients between m_i and E_{Ni} were found to be highly significant (p < 0.01) with r = 0.84, 0.87 and 0.91 for MIL, SLD and SVD fabric measures respectively. **Figure 11d-f** show the relation between G_{Nij} and $m_i m_j$ with correlation coefficients r = 0.81-0.86 at p < 0.01. The correlation coefficients between ν_{ij} and m_j/m_i were slightly lower (r= 0.72-0.73), but still highly significant at p < 0.01 (**Figure 11g-i)**. These results clearly demonstrate that a strong relationship exists between morphology characterized by fabric tensors and the orthotropic elastic properties obtained from μFE homogenization and establish the basis for evaluating the orthotropic morphology-elasticity model (Zysset and Curnier, 1995) for snow.

3.4 Morphology-elasticity model fits for snow

The results of multiple linear regression analysis for ISO and ZC models for both compliance and stiffness approaches are presented in **Table 4A**. Neglecting fabric information and using an isotropic power law model yielded r^2_{adj} of 0.81 and 0.89 with associated mean model norm errors of 40% and 43% for compliance and stiffness fits respectively. Depending on the fabric measure used, the ZC model provided r^2_{adj} in the range of 0.85-0.87 and mean NE^{model} in the range of 30-31% for compliance fits. In contrast, when applied on the stiffness tensor, the ZC model explained about 97% of the variation of stiffness components with associated mean NE^{model} in the range of 27-29%. The plots between μFE computed and predicted components of both the compliance and stiffness tensors are shown in **Figure 12**. The histograms of model norm errors are also compared in **Figures 13a and 13b** which clearly indicate the better predictive power of ZC model with lower relative norm errors as compared to ISO model for both the compliance and stiffness approaches. Interestingly, the regression results suggest that the ISO and ZC models better described the data when used with stiffness tensor components in comparison to the compliance approach. In the present study, the distribution of compliances was found to be more skewed (Skewness=5.3) compared to the distribution of stiffness components (Skewness=3.1) which might have resulted in more optimal weighting of data in relationships based on stiffness approach.

The histograms of the residuals of stiffness tensor components (**Figure 14**) indicate that the estimation errors are approximately normally distributed. Compared to ISO model, the ZC model resulted in significant improvement with approximately 42-48% reduction in standard deviation of the residuals of stiffness tensor components. The model performance was further evaluated for the prediction of individual orthotropic engineering constants (E_i, G_{ij} and ν_{ij}) using the stiffness approach. Depending on the fabric measure used, the ZC model could explain about 96-97% of the variations in E_i, 94-97% of the variations in G_{ij} and 52-63% of the variations in ν_{ij} **(Table 4A)**. In contrast, the ISO model shows no correlation with ν_{ij} and explained about 84% of the variations in E_i and about 94% of the variation in G_{ij}. A comparison between predicted engineering constants from the two models (ZC with SVD fabric and isotropic) and those calculated from the μFE analyses are shown in **Figure 15**.

The model parameters for the compliance and stiffness fits are shown in **Table 4B** and **4C** respectively. The values of ZC model constants $\{E_0, \nu_0, G_0\}$ and $\{\lambda_0, \lambda_0', G_0\}$ in Table 4C satisfy the relations $G_0 \approx \frac{E_0}{2(1+\nu_0)}$ and $\lambda_0 \approx \lambda_0'$ and can be interpreted as the elastic properties of an extrapolated isotropic solid with $\upsilon_s = 1$ and $m_i = 1$. Considering the wide range of densities and snow classes used in this study, the order of magnitude of E_0 and G_0 compares well with the Young's modulus (9.5 GPa) and shear modulus (3.57 GPa) of ice. The exponent l varied between [0.63-0.66] for SVD fabric tensor and between [2.36-2.64] for SLD and MIL measures. Since SVD measure uses length dimensions cubed, the amplified differences between the major and minor components in the directional distribution data resulted in lower values of exponent l corresponding to SVD fabric.

The estimates of exponent k of ice volume fraction for ZC and ISO models were in the range of [4.32-4.48] and [4.51-4.71] for compliance and stiffness fits respectively. Applying theory of propagation of uncertainty to an isotropic model fit of the form $E \sim \nu_s^k$ yields a uncertainty scaling relation as $(E)_{CV} = k(\nu_s)_{CV}$. The estimates of exponent k match very closely with the variability scaling parameter γ = 4.56 [4.41-4.70] obtained from analysis of statistical uncertainties of the μFE results **(Figure 5d)** and establishes the appropriateness of power law dependence on ice volume fraction in both ISO and ZC models. The exponent of snow density in previously published power law relations of Young's modulus varied between 2.94 (based on high frequency cyclic loading experiments in Sigrist, 2006) to 6.6 (obtained via numerical simulations, Hagenmuller et al., 2014a).

The strong non-linearity between Young's modulus and ice volume fraction (or density) is at variance with the prediction of quadratic dependence on solid volume fraction for periodic open-cell solids with regular arrangement of isotropic cells (Gibson and Ashby, 1997). The deviations from quadratic dependence for random open-cell porous solids have been related with large scatter in strut-thickness distribution, imperfections, irregularities, or anisotropy in the cell arrangements (Guessasma et al., 2008; Andrews et al., 1999). Numerical simulations (Guessasma et al., 2008) provided values of volume fraction exponent as high as 3.97±0.47 for a disordered open cell solid model consisting of overlapping spherical pores with solid volume fraction in the range 0.1-0.38. Compared to architecturally optimized cellular materials like metallic foams or honeycomb structures, the 3D microstructure of various snow classes is highly disordered and is reflected in many dead-ends existing in the ice matrix which do not contribute to the stress pathways (Theile, 2011). Thus, the non-uniform stress distribution in the tortuous matrix of disordered open cell solids reduces their stiffness which is reflected in values of exponent $k > 2$. The values of exponent k obtained in this study are within the range reported in previous experimental (Sigrist, 2006) and numerical studies (Hagenmuller et al. 2014a) on snow and are consistent with those reported for disordered open cell solids (Guessasma et al., 2008).

In general, the study shows that ice volume fraction along with fabric tensors is a very good predictor of the anisotropic stiffness tensor of snow. Our results (**Figures 11 and 12, Tables 4**) also suggest that the choice of volume (SVD, SLD) or surface (MIL) based fabric measures does not affect the prediction of elastic properties in a systematic way; all three provide a good representation of the mechanical characteristic of the snow fabric. Overall, the ZC model consistently performed better than the ISO model, producing higher correlation coefficients of determination, lower relative norm errors and smaller dispersion of residuals for the prediction of stiffness tensor components as a whole as well as for individual elastic constants. The recently introduced microstructural indicator, the minimum cut density, also showed excellent correlation ($r^2 = 0.97$) with anisotropic Young's moduli (Hagenmuller et al., 2014a). However, its association with all the components of the stiffness tensor is not yet clear.

This study has a few limitations. It is known that discretisation errors can lead to overestimated stiffness values as a function of resolution in μFE models (Arns et al. 2002). For three-dimensional random open cell solids, the discretisation errors have been shown to be less than 10% if the strut thickness is covered by a minimum of four voxels (Roberts and Garboczi, 2002). Depending on the mean ice thickness (h_{ice}) and resolutions for individual samples (Table 1), a discretization of four to seventeen voxels per ice structure thickness was achieved which approximately meets the previously proposed criteria by Roberts and Garboczi (2002). By assuming an isotropic and homogeneous Young's modulus of ice at the matrix level, the predicted elastic properties are related exclusively to the microstructural-fabric of snow and all matrix level effects such as degree of sintering or micro-damage in ice matrix are ignored.

It is interesting to note that despite high correlations, significant uncertainties still exist in the prediction of stiffness tensor for individual snow samples. The relative norm errors associated with the isotropic model range between 20% and 108%, while those associated with the ZC model range between 2% and 79%. The uncertainties in the predicted results may not only be due to the occurrence of artefacts in both the fabric tensor and FE-based mechanical assessments (boundary conditions and voxelized mesh) but also due to the insufficient resolution of the images as well as an inherent inadequacy of second-order fabric tensors in characterizing the full mechanical significance of the microstructure. The effect of low scale variability or disorderness of the snow microstructure in the μFE models is essentially lost by the stereological averaging process involved in the computation of second-rank fabric tensors. The prediction error may be partially reduced by increasing the resolution of the microstructure images, but we expect the local variability or randomness of the snow microstructure to remain a major limitation for second-rank fabric tensor based morphology-elasticity model.

Further, the experimental determinations of Young's modulus of snow (Mellor, 1975; Frolov and Fedyukin, 1998; Scapozza and Bartelt, 2003; Sigrist, 2006) are also associated with considerable scatter of at least similar magnitude. The fabric-elasticity relationships obtained in this study, on the other hand, predict not only uniaxial Young's moduli, but also include full orthotropic stiffness and compliance tensors which characterize the elastic response of snow to any possible loading.

4. Conclusion

The inter-linking of the elastic properties of snow with its density and microstructure plays a key role in understanding the microstructural causes of slab avalanche release mechanisms. The homogenized orthotropic stiffness tensors of the snow samples were computed using X-ray µCT derived high resolution digital µFE models. The maximum available cubic image volume for each sample fulfilled the RVE criteria with respect to the homogenized stiffness tensor except for low density new snow samples. The $RVE_{elastic}$ is found to be directly linked with $RVE_{structure}$ via a linear scaling relation, $\left(E_{eff}\right)_{CV} = \gamma(\upsilon_s)_{CV}$, which can be used to *a priori* decide about the $RVE_{elastic}$ with acceptable level of microstructural and property uncertainties. The estimates of exponent k of ice volume fraction for isotropic ($k = 4.34$) and orthotropic ($k = 4.48$) models match very closely with the variability scaling parameter $\gamma = 4.56$. The study shows that effective isotropic Young's moduli and Poisson ratio's, derived from µFE computed orthotropic stiffness and compliance tensors, compare quite well with previously published results thereby validating the numerical modelling approach adopted. The anisotropic elastic properties computed from µFE analysis essentially reflect the mechanical properties of snow due to its microstructure and are not affected by experimental artifacts. Multiple linear regressions of the ice volume fraction based isotropic model and the results of µFE analysis explained up to 89% of the variability in stiffness tensor components with associated mean relative norm error of 43.2%. Accounting for microstructural fabric in ZC model raised the adjusted coefficient of determination r^2_{adj} to 97% with a mean model norm error of 28.4%. The standard deviation of the residuals of stiffness tensor components also considerably reduced by 42-48% with the introduction of fabric tensors in ZC model. In terms of which fabric measure to employ, the study found no systematic variation in the performance of volume- and surface-based fabric tensors and all three fabric measures could reasonably explain the anisotropic elastic properties of snow.

In conclusion, the fabric-elasticity relations obtained in this study can be used to predict the homogenized elastic properties of snow by measuring ice volume fraction and fabric descriptors through high resolution X-ray μCT imaging; an approach which is several order of magnitude more computationally cost effective in comparison to μFE based homogenization. For future work, a systematic study on a larger set of samples covering a wider density and snow type range could provide more refined morphology-elasticity model constants. Since stiffness and ultimate strength of snow have been shown to be highly correlated (Hagenmuller et al., 2014b), this approach shows promise for extension to the prediction of post-elastic behaviour.

Acknowledgments

Funding from the UKIERI (project reference UKUTP201100164) and the use of Eddie Linux compute cluster for carrying out the FE simulations at Edinburgh Compute and Data Facility, University of Edinburgh is acknowledged. The first author is specially grateful to Dr Pankaj Pankaj for his continuous support and insightful discussions. Special thanks to Dr E. J. Garboczi for providing the parallel version of the FE code and Sh A. Ganju for critical comments. The authors also thank Sh. Paramvir Singh and Sh. Vinod Kumar for their contribution in 3D image acquisition and data pre-processing.

References

Andrews, E., Sanders, W.L., Gibson, L.J., 1999. Compressive and tensile behaviour of aluminium foams. Mat. Sci. Eng. A-Struct. 270, 113-124.

Arns, C.H., Knackstedt, M.A., Pincewski, W.V., Garboczi, E.J., 2002. Computation of linear elastic properties from microtomographic images: methodology and agreement between theory and experiment. Geophysics 67, 1396-1405.

Bohn, R.B., Garboczi, E.J, 2003. User Manual for Finite Element and Finite Difference Programs: A Parallel Version of NISTIR-6269. NIST Internal Report 6997.

Calonne, N., Flin, F., Morin, S., Lesare, B., Roscoat, S.R.D., Geindreau, C., 2011. Numerical and experimental investigations of the effective thermal conductivity of snow. Geophys. Res. Lett. 38, L23501.

Camponovo, C., Schweizer, J., 2001. Rheological measurements of the viscoelastic properties of snow. Ann. Glaciol. 32, 44-50.

Chandel, C., Srivastava, P.K., Mahajan, P., 2014. Micromechanical analysis of deformation of snow using X-ray tomography. Cold Reg. Sci. Technol. 101, 14-23.

Cowin, C., 1985. The relationship between the elastic tensor and the fabric tensor. Mech. Mater. 4, 137-147.

Cowin, S.C., Yang, G., Mehrabadi, M.M., 1999. Bounds on the effective anisotropic elastic constants. J. Elasticity 57, 1-24.

Cruz-Orive, L.M., Karlsson, L.M., Larsen, S.E., Wainschtein, F., 1992. Characterizing anisotropy: a new concept. Micron Microscopica Acta 23, 75-76.

Fierz, C., Armstrong, R.L., Durand, Y., Etchevers, P., Greene, E. M., McClung, D.M., Nishimura, K., Satyawali, P.K., Sokratov, S.A., 2009. The international classification for seasonal snow on the ground. Technical report. IHP-VII Technical Documents in Hydrology N83, IACS Contribution N1, UNESCO-IHP. Paris.

Frolov, A.D., Fedyukin, I.V., 1998. Elastic properties of snow-ice formation in their whole density range. Ann. Glaciol. 26, 55-58.

Garboczi, E.J., Day, A.R., 1995. An algorithm for computing the effective linear elastic properties of heterogeneous material: Three-dimensional results for composites with equal phase Poisson ratios. J. Mech. Phy. Solids 43, 1349-1362.

Gaume, J., Chambon, G., Eckert, N., Naaim, M., Schweizer, J., 2015a. Influence of weak layer heterogeneity and slab properties on slab tensile failure propensity and avalanche release area. The Cryosphere, 9, 795-804, doi:10.5194/tc-9-795-2015.

Gaume, J., van Herwijnen, A., Chambon, G., Birkeland, K. W., Schweizer, J., 2015b. Modeling of crack propagation in weak snowpack layers using the discrete element method. The Cryosphere, 9, 1915-1932, doi:10.5194/tc-9-1915-2015.

Gibson, L.J., Ashby, M.F., 1997. Cellular solids: structure and properties. second ed., Cambridge University Press, Cambridge.

Guessasma, S., Babin, P., Valle, G.D., Dendievel, R., 2008. Relating cellular structure of open solid food foams to their Young's modulus: finite element calculation. Int. J. Solids Struct. 45, 2881-2896.

Habermann, M., Schweizer, J., Jamieson, J.B., 2008. Influence of snowpack layering on human-triggered snow slab avalanche release. Cold Reg. Sci. Technol. 54(3), 176-182.

Hagenmuller, P., Calonne, N., Chambon, G., Flin, F., Geindreau, C., Naaim, M., 2014a. Characterization of the snow microstructural bonding system through the minimum cut density. Cold Reg. Sci. Technol. 108, 72-79.

Hagenmuller, P., Theile, T., Schneebeli, M., 2014b. Numerical simulation of microstructural damage and tensile strength of snow. Geophys. Res. Lett. 41, 86-89.

Harrigan, T.P., Mann, R.W., 1984. Characterization of microstructural anisotropy in orthotropic materials using a second rank tensor. J. Mater. Sci. 19, 761-767.

Heierli, J., Gumbsch, P., Zaiser, M., 2008. Anticrack nucleation as triggering mechanism for snow slab avalanches. Science 321, 240–243.

Hildebrand, T., Ruegsegger, P., 1997. A new method for the model-independent assessment of thickness in three-dimensional images. J. Microsc. 185, 67-75.

Hill, R., 1952. The elastic behaviour of crystalline aggregate. Proc. Phys. Soc. A 65, 349-354.

Huet, C., 1990. Application of variational concepts to size effects in elastic heterogeneous bodies. J. Mech. Phys. Solids 38, 813-841.

Kanatani, K., 1984. Distribution of directional data and fabric tensors. International Journal of Engineering Science 22, 149-164.

Ketcham, R.A., Ryan, T., 2004. Quantification and visualization of anisotropy in trabecular bone. J. Microsc. 213, 158-171.

Kochle, B., Schneebeli, M., 2014. Three-dimensional microstructure and numerical calculation of elastic properties of alpine snow with a focus on weak layers. J. Glaciol. 60(222), 705-713.

Kuo, C.Y., Frost, J.D., Chameau, J.L.A., 1998. Image analysis determination of stereology based fabric tensors. Geotechnique. 48(4), 515-525.

Lorensen, W.E., Cline, H.E., 1987. Marching cubes: a high resolution 3D surface construction algorithm. Comp. Graphics 21, 163-169.

Mahajan, P., Kalakuntla, R., Chandel, C., 2010. Numerical simulation of failure in a layered thin snowpack under skier load. Ann. Glaciol. 51, 169-175.

McClung, D.M., 1996. Effects of temperature on fracture in dry slab avalanche release. J. Geophys. Res. 101(B10), 21907-21920. doi:10.1029/95JB03114.

McClung, D.M., 2005. Dry slab avalanche shear fracture properties from field measurements. J. Geophys. Res. 110(F4), F04005. doi: 10.1029/2005JF000291.

Mellor, M., 1975. A review of basic snow mechanics. IAHS-AISH Publication No. 114, 251-291.

Mellor, M., 1977. Engineering properties of snow. J. Glaciol. 19, 15-66.

Nemat-Nasser, S., Hori, M., 1998. Micromechanics: overall properties of heterogeneous materials. second ed., North-Holland. Netherlands.

Niezgoda, S.R., Turner, D.M., Fullwood, D.T., Kalidindi, S.R., 2010. Optimized structure based representative volume element sets reflecting the ensemble-averaged 2-point statistics. Acta Mater. 58, 4432-4445.

Ostoja-Starzewski, M., 2008. Microstructural randomness and scaling in mechanics of materials. Chapman & Hall/CRC/Taylor & Francis, Boca Raton (FL).

Reiweger, I., Schweizer, J., 2010. Failure of a layer of buried surface hoar. Geophys. Res. Lett. 37, L24501. doi: 10.1029/2010GL045433.

Reiweger, I., Gaume, J., Schweizer, J., 2015. A new mixed-mode failure criterion for weak snowpack layers. Geophys. Res. Lett. 42, 1427-1432, doi:10.1002/2014GL062780.

Rietbergen, B.V., Odgaard, A., Kabel, J., Huiskcs, R., 1996. Direct elastic assessment of mechanical symmetries and properties of trabecular bone architecture. J Biomech. 29, 1653-1657.

Roberts, A.P., Garboczi, E.J., 2002. Computation of the linear elastic properties of random porous materials with a wide variety of microstructure. Proc. R. Soc. A 458, 1033-1054.

Sanderson, T.J.O., 1988. Mechanical properties of ice: laboratory studies, in T.J.O. Sanderson (Eds.), Ice mechanics: risks to offshore structures, Graham and Trotman, London, pp. 70-103.

Scapozza, C., Bartelt. P., 2003. Triaxial tests on snow at low strain rate. Part II. Constitutive behaviour. J. Glaciol. 49, 91-101.

Schneebeli, M., 2004. Numerical simulation of elastic stress in the microstructure of snow. Ann. Glaciol. 38, 339-342.

Schweizer, J., Jamieson, J.B., Schneebeli, M., 2003. Snow avalanche formation. Rev. Geophys. 41, 1016-41. doi:10.1029/2002RG000123.

Shapiro, L.H., Johnson, J.B., Sturm, M., Blaisdell, G.L., 1997. Snow mechanics: review of the state of knowledge and applications. Tech. Rep. 97-3, CRREL.

Shertzer, R.H., Adams, E.E., 2011. Anisotropic thermal conductivity model for dry snow. Cold Reg. Sci. Technol. 69, 122-128.

Sigrist, C., 2006. Measurement of the fracture mechanical properties of snow and application to dry snow slab avalanche release. Ph.D. dissertation, Diss. ETH No. 16736, Swiss Fed. Inst. of Technol., Zurich.

Sigrist, C., Schweizer, J., 2007. Critical energy release rates of weak snowpack layers determined in field experiments. Geophysical Research Letters 34, L03502. doi:10.1029/2006GL028576.

Smit, T.H, Schneider, E., Odgaard, A., 1998. Star length distribution: a volume-based concept for the characterization of structural anisotropy. J. Microsc. 191 249-257.

Smith, N., 1969. Determining the dynamic properties of snow and ice by forced vibration. Tech. Rep. 216, CRREL.

Srivastava, P.K., Mahajan, P., Satyawali, P.K., Kumar, V., 2010. Observation of temperature gradient metamorphism in snow by X-ray computed microtomography:

measurement of microstructure parameters and simulation of linear elastic properties. Ann. Glaciol. 50, 73-82.

Swaminathan, S., Ghosh, S., Pagano, N.J., 2006. Statistically equivalent representative volume elements for unidirectional composites microstructures: Part I – without damage. J. Compos. Mater. 40, 583-604.

Theile, T., Lowe, H., Theile, T.C., Schneebeli, M., 2011. Simulating creep of snow based on microstructure and the anisotropic deformation of ice. Acta Mater. 59, 7104-7113.

Whitehouse, W.J., 1974. The quantitative morphology of anisotropic trabecular bone. J. Microsc. 101, 153-168.

Xu, X.F., Chen, X., 2009. Stochastic homogenization of random elastic multi-phase composites and size quantification of representative volume element. Mech. Mater. 41, 174-186.

Yoon, Y.G., Yang, G., Cowin, S.C., 2002. Estimation of the effective transversely isotropic elastic constants of a material from known values of the material's orthotropic elastic constants. Biomech. Model. Mechanobiol. 1, 83-93.

Yuan, H., Lee, J.H., Guilkey, J.E., 2010. Stochastic reconstruction of the microstructure of equilibrium form snow and computation of effective elastic properties. J. Glaciol. 56(197), 405-414.

Zysset, P.K., Curnier, A., 1995. An alternative model for anisotropic elasticity based on fabric tensors. Mech. Mater. 21, 243-250.

Zysset, P.K., 2003. A review of morphology-elasticity relationships in human trabecular bone: theories and experiments. J. Biomech. 36, 1469-1485.

Table 1: Description of the snow samples used in this study. PP: precipitation particles, RG: rounded grains, DF: decomposing and fragmented precipitation particles, FC: faceted crystals, DH: depth hoar, υ_s: ice volume fraction, $\boldsymbol{\rho_s}$: snow density, $\delta := L/h_{ice}$ and δ' $:= L/h_{pore}$, where h_{ice} is the mean ice thickness and h_{pore} is the mean pore thickness.

Sample	Snow Class	Resolution (μm)	Image volume L^3 (mm^3)	υ_s	ρ_s (kgm^{-3})	h_{ice} (mm)	h_{pore} (mm)	δ	δ'
ET1	RG	19.87	5.96^3	0.436	400	0.236	0.212	25.3	28.2
G1	DF	23.89	7.17^3	0.212	194	0.149	0.376	48.0	19.1
G2	DH	25.69	7.71^3	0.347	319	0.267	0.449	28.9	17.2
G3	FC	23.89	7.17^3	0.344	315	0.228	0.374	31.5	19.2
G4	DH	23.89	7.17^3	0.382	350	0.339	0.507	21.1	14.1
HF1	RG	25.69	7.71^3	0.401	368	0.140	0.159	55.2	48.5
HF2	FC	25.69	7.71^3	0.455	418	0.144	0.156	53.6	49.4
HF3	FC	25.69	7.71^3	0.466	427	0.143	0.164	53.8	47.1
HF4	FC	25.69	7.71^3	0.467	428	0.153	0.182	50.5	42.4
HF5	DH	25.69	7.71^3	0.449	412	0.155	0.201	49.7	38.4
HF6	DH	25.69	7.71^3	0.438	402	0.150	0.216	51.3	35.7
HF7	DH	25.69	7.71^3	0.443	406	0.156	0.224	49.4	34.5
KFC1	FC	31.85	9.55^3	0.338	310	0.378	0.562	25.3	17.0
KFC2	FC	31.85	9.55^3	0.274	251	0.381	0.614	25.1	15.6
M1	PP	25.69	7.71^3	0.106	97	0.105	0.473	73.1	16.3
M2	PP	17.13	5.14^3	0.142	130	0.101	0.421	51.1	12.2
MTS1	RG	23.89	7.17^3	0.234	214	0.118	0.283	60.9	25.3
S1	RG	25.69	7.71^3	0.349	320	0.239	0.320	32.2	24.1
S2	RG	25.69	7.71^3	0.408	374	0.259	0.279	29.7	27.7
S3	FC	25.69	7.71^3	0.357	327	0.446	0.476	17.3	16.2
S4	FC	25.69	7.71^3	0.433	397	0.398	0.452	19.4	17.1
S5	RG	25.69	7.71^3	0.395	362	0.310	0.367	24.9	21.0
T1	RG	25.69	7.71^3	0.460	422	0.217	0.211	35.5	36.6
T2	RG	25.69	7.71^3	0.581	533	0.217	0.150	35.6	51.2
T3	RG	25.69	7.71^3	0.444	407	0.318	0.309	24.3	24.9

Table 2: Normalized eigenvalues **(**m_1, m_2, m_3**)** of the SVD, SLD and MIL derived fabric ellipsoids.

	SVD			SLD			MIL		
Sample	$\mathbf{m_1}$	$\mathbf{m_2}$	$\mathbf{m_3}$	$\mathbf{m_1}$	$\mathbf{m_2}$	$\mathbf{m_3}$	$\mathbf{m_1}$	$\mathbf{m_2}$	$\mathbf{m_3}$
ET1	0.355	0.340	0.305	0.339	0.335	0.326	0.336	0.334	0.330
G1	0.349	0.333	0.318	0.339	0.332	0.329	0.337	0.333	0.330
G2	0.351	0.332	0.317	0.338	0.334	0.329	0.338	0.333	0.329
G3	0.357	0.338	0.305	0.340	0.334	0.326	0.337	0.333	0.330
G4	0.405	0.301	0.294	0.351	0.327	0.322	0.349	0.326	0.325
HF1	0.355	0.345	0.300	0.341	0.335	0.323	0.340	0.331	0.329
HF2	0.448	0.291	0.261	0.358	0.325	0.317	0.357	0.323	0.320
HF3	0.503	0.256	0.241	0.373	0.316	0.312	0.366	0.318	0.316
HF4	0.480	0.272	0.248	0.369	0.320	0.312	0.370	0.317	0.313
HF5	0.499	0.256	0.245	0.374	0.315	0.311	0.369	0.317	0.314
HF6	0.487	0.260	0.253	0.369	0.317	0.314	0.363	0.320	0.317
HF7	0.473	0.272	0.255	0.366	0.319	0.315	0.366	0.319	0.315
KFC1	0.380	0.330	0.290	0.336	0.334	0.330	0.347	0.329	0.324
KFC2	0.415	0.303	0.282	0.348	0.330	0.322	0.348	0.329	0.322
M1	0.399	0.336	0.265	0.348	0.333	0.319	0.340	0.338	0.322
M2	0.381	0.348	0.271	0.344	0.336	0.321	0.341	0.336	0.323
MTS1	0.359	0.333	0.308	0.339	0.335	0.325	0.336	0.333	0.331
S1	0.363	0.346	0.291	0.344	0.340	0.316	0.339	0.337	0.324
S2	0.382	0.356	0.262	0.350	0.341	0.309	0.342	0.336	0.322
S3	0.409	0.318	0.274	0.346	0.332	0.322	0.352	0.325	0.323
S4	0.411	0.309	0.280	0.347	0.329	0.324	0.340	0.331	0.329
S5	0.360	0.348	0.293	0.344	0.341	0.315	0.340	0.340	0.320
T1	0.350	0.328	0.322	0.337	0.334	0.329	0.341	0.332	0.327
T2	0.369	0.340	0.292	0.341	0.336	0.323	0.343	0.331	0.326
T3	0.368	0.346	0.287	0.343	0.336	0.321	0.338	0.332	0.330

Table 3: Summary of the orthotropic elastic parameters E_i (MPa), G_{ij} (MPa), and ν_{ij} obtained by μFE analysis.

Sample	E_1	E_2	E_3	G_{12}	G_{13}	G_{23}	ν_{12}	ν_{21}	ν_{13}	ν_{31}	ν_{23}	ν_{32}
ET1	452.1	357.2	296.1	174.2	153.4	138.8	0.22	0.17	0.24	0.16	0.21	0.18
G1	25.1	15.9	14.1	6.8	8.7	6.2	0.13	0.09	0.29	0.17	0.19	0.17
G2	104.0	97.8	78.2	44.1	40.2	44.0	0.20	0.19	0.18	0.13	0.25	0.20
G3	126.4	85.5	68.4	44.8	39.9	36.8	0.20	0.13	0.23	0.12	0.19	0.15
G4	166.8	94.2	89.2	48.9	60.2	46.7	0.19	0.11	0.26	0.14	0.19	0.18
HF1	416.3	357.2	355.0	160.3	160.7	147.2	0.21	0.18	0.21	0.18	0.18	0.18
HF2	901.6	505.9	475.4	287.9	276.2	208.4	0.27	0.15	0.27	0.14	0.19	0.18
HF3	1005.5	462.5	459.0	288.6	282.6	199.3	0.27	0.12	0.27	0.12	0.19	0.19
HF4	1071.1	465.7	454.3	292.2	289.1	194.1	0.26	0.11	0.27	0.12	0.19	0.18
HF5	1013.5	413.7	406.1	269.9	269.6	172.6	0.28	0.12	0.27	0.11	0.18	0.18
HF6	940.6	389.0	386.5	255.6	247.9	165.6	0.27	0.11	0.26	0.11	0.19	0.19
HF7	1001.1	401.9	377.2	265.8	253.5	163.8	0.28	0.11	0.27	0.10	0.20	0.18
KFC1	146.7	127.2	95.3	58.9	48.6	46.1	0.21	0.18	0.16	0.10	0.19	0.14
KFC2	107.0	79.7	57.8	37.9	31.4	24.6	0.22	0.16	0.32	0.17	0.16	0.12
M1	1.2	0.9	0.8	0.6	0.3	0.5	0.19	0.14	0.09	0.06	0.14	0.14
M2	2.0	1.6	1.2	0.8	0.7	0.6	0.14	0.12	0.27	0.17	0.16	0.12
MTS1	72.3	52.5	37.6	25.9	22.7	19.4	0.23	0.17	0.30	0.16	0.23	0.17
S1	239.5	189.7	180.0	88.0	86.7	79.3	0.21	0.16	0.23	0.17	0.19	0.18
S2	451.9	403.9	391.2	183.7	182.8	171.5	0.20	0.18	0.22	0.19	0.19	0.19
S3	279.2	114.6	100.3	71.0	73.3	39.3	0.24	0.10	0.35	0.13	0.13	0.12
S4	547.6	297.0	293.1	164.2	167.0	131.2	0.22	0.12	0.27	0.14	0.20	0.20
S5	364.6	334.1	303.5	142.3	139.3	135.6	0.19	0.17	0.21	0.17	0.20	0.18
T1	749.8	646.7	620.0	291.5	285.3	267.2	0.22	0.19	0.22	0.18	0.20	0.19
T2	1944.9	1912.2	1650.0	781.5	755.7	727.2	0.21	0.21	0.25	0.21	0.22	0.19
T3	480.6	471.2	423.6	199.1	194.7	189.5	0.19	0.19	0.21	0.19	0.20	0.18

Table 4: (A) r^2_{adj} and mean model norm error (NE^{model}) computed for compliance ($\boldsymbol{S}_{ijkl}$) and stiffness ($\boldsymbol{C}_{ijkl}$) tensor components as well as individual orthotropic engineering constants (E_i, G_{ij} and ν_{ij}). The compliance approach was based on equation 6 and 8 while stiffness approach was based on equation 7 and 9. Entries marked 'n.s' indicate non-significant correlation. Model parameters and 95% confidence intervals for compliance and stiffness approaches are shown in **(B)** and **(C)** respectively.

(A)		Compliance approach ($\boldsymbol{S}_{ijkl}$)		Stiffness approach ($\boldsymbol{C}_{ijkl}$)		E_i (MPa)	G_{ij} (MPa)	ν_{ij}
Model	Fabric	r^2_{adj}	NE^{model} (%)	r^2_{adj}	NE^{model} (%)	r^2_{adj}	r^2_{adj}	r^2_{adj}
ZC	SVD	0.86	30.1	0.97	27.4	0.97	0.97	0.63
	SLD	0.87	31.1	0.97	28.3	0.96	0.97	0.60
	MIL	0.85	30.0	0.97	29.4	0.96	0.94	0.52
ISO	-	0.81	40.4	0.89	43.2	0.84	0.94	n.s.

(B)	ZC						ISO	
Fabric	SVD		SLD		MIL		-	
	Value	95% CI	Value	95% CI	Value	95% CI	Value	95% CI
E_0 (GPa)	15.87	13.80 - 18.26	15.44	13.44 - 17.75	15.30	13.29 - 17.62	18.05	15.98 - 20.39
ν_0	0.176	0.174 - 0.178	0.176	0.174 - 0.178	0.176	0.174 - 0.178	-	-
G_0 (GPa)	6.76	5.87 - 7.77	6.57	5.72 - 7.55	6.51	5.65 - 7.49	7.65	6.65 - 8.79
k	4.34	4.23 - 4.45	4.33	4.22 - 4.44	4.32	4.21 - 4.43	4.48	4.37 - 4.59
l	0.63	0.45 - 0.80	2.64	1.93 - 3.36	2.36	1.65 - 3.08	-	-

(C)	ZC						ISO	
Fabric	SVD		SLD		MIL		-	
	Value	95% CI	Value	95% CI	Value	95% CI	Value	95% CI
λ_0 (GPa)	5.54	4.79 - 6.40	5.38	4.65 - 6.22	5.33	4.61 - 6.16	4.43	4.17 - 4.70
λ'_0 (GPa)	5.48	4.80 - 6.25	5.32	4.66 - 6.01	5.27	4.62 - 6.02	-	-
G_0 (GPa)	9.92	8.58 - 11.46	9.63	8.33 - 11.14	9.54	8.25 - 11.04	7.90	6.87 - 9.09
k	4.71	4.60 - 4.82	4.70	4.58 - 4.81	4.69	4.58 - 4.80	4.51	4.40 - 4.62
l	0.66	0.47 - 0.84	2.58	1.83 - 3.32	2.55	1.82 - 3.29	-	-

Revised Figure(s)

Figure Captions

Figure 1: Reconstructed 3D microstructure of representative snow classes; PP (Sample M2), RG (sample S2), FC (sample KFC2) and DH (sample HF5).

Figure 2: Voigt and Reuss bounds on effective isotropic bulk (k_{eff}) and shear (G_{eff}) modulus computed on the full image volumes for all the samples

Figure 3: Partitioning procedure to generate three sets of cubical sub-volumes of different edge lengths (L) for investigating the statistical variability. **(a)** set of 8 cubes with L=150 voxels, **(b)** set of 27 cubes with L=100 voxels, and **(c)** set of 64 cubes with L=75 voxels.

Figure 4: Plots showing convergence of **(a)** ice volume fraction (υ_s), **(b)** Effective Young's modulus (E_{eff}), and **(c)** norm of orthotropic stiffness tensor ($\|\boldsymbol{C}_{FE_{ortho}}\|$), computed on concentric cubic snow volumes of increasing sizes.

Figure 5: Variation of mean E_{eff} versus mean υ_s for cubical sub-volumes with edge length (L) of **(a)** 75 voxels, **(b)** 100 voxels, and **(c)** 150 voxels. The error bars represent ±one standard deviation. The linear scaling relation showing the correlation between relative variability of a microstructural measure, $(\upsilon_s)_{CV}$, and effective property, $\left(E_{eff}\right)_{CV}$, is shown in **(d)**. Depending on the resolution of individual images, the cube edge lengths of 150 voxel, 100 voxel and 75 voxel translated into physical edge lengths of 2.6-4.8 mm, 1.7-3.2 mm and 1.3-2.4 mm respectively and $\delta := L/l_{micro}$.

Figure 6: (a) Comparison of E_{eff} with previously published results. Dynamic measurements (A and B) and strain-rate and creep tests results (C) are from Shapiro et al. (1997). µFE simulations based exponential fit (D) from Kochle and Schneebeli, (2014), Laboratory measurements form Scapozza and Bartelt, (2003), (E), and Sigrist et al. (2006), (F), are also included. Open symbols correspond to simulations over sub-volumes with edge length, L=150 voxels, while filled symbols represents results from the full image volume, i.e. L=300 voxels.

Figure 6: (b) Scatter plot of ν_{eff} with density. Open symbols correspond to simulations over sub-volumes with edge length, L=150 voxels, while light filled symbols represents results from the full image volume, i.e. L=300 voxels. For comparison, µFE results (dark filled symbols) from Kochle and Schneebeli (2014) and measurements (region D) from Smith (1969) are also included.

Figure 7: Bivariate plots of elongation index (EI) vs. isotropic index (I) for (a) SVD, (b) SLD and (c) MIL fabric tensors respectively. The corresponding plot between mechanical elongation (EI_{Mech}) and isotropy (I_{Mech}) indices is shown in (d).

Figure 8: Ternary shape diagram of isotropy and elongation indices derived from SVD fabric measures.

Figure 9: Fabric and mechanical anisotropy indices v/s ice volume fraction

Figure 10: Fabric tensor and orthotropic stiffness tensor ($\boldsymbol{C}_{ijkl}$) representations of snow samples depicted in Figure 1. The top and middle row depicts fabric ellipsoids for SVD and MIL fabric tensors while the bottom row shows the geometrical representations of $\boldsymbol{C}_{ijkl}$ for PP, RG, FC and DH snow classes. The fabric tensors are shown in the original image coordinate system which matches closely with the mechanical main directions obtained via the optimization procedure.

Figure 11: Correlation between normalized orthotropic technical constants ($E_{Ni,}$ $G_{Nij,}$ ν_{ij}) and functions of eigenvalues (m_i) corresponding to MIL, SLD and SVD fabric measures.

Figure 12: Correlation between µFE computed and predicted components of **(a)** compliance, and **(b)** stiffness tensors using the (i) Zysset-Curnier (ZC) model with SVD, SLD and MIL fabric measures, and (ii) isotropic model.

Figure 13: Histograms of model norm errors for **(a)** compliance and **(b)** stiffness approaches. Compared to ISO model, the ZC model produced 24-36% lower relative model norm errors.

Figure 14: Histograms of residuals of stiffness tensor components for ZC model with SVD, SLD and MIL fabric measures and Isotropic model. Residuals are approximately normally distributed. ZC model appears to perform better with lower mean values and standard deviation of the residuals.

Figure 15: Comparison between µFE computed and predicted engineering constants (E_i, G_{ij}, ν_{ij}) using (i) ZC model with SVD fabric tensor (top row) and, (ii) isotropic model (bottom row).

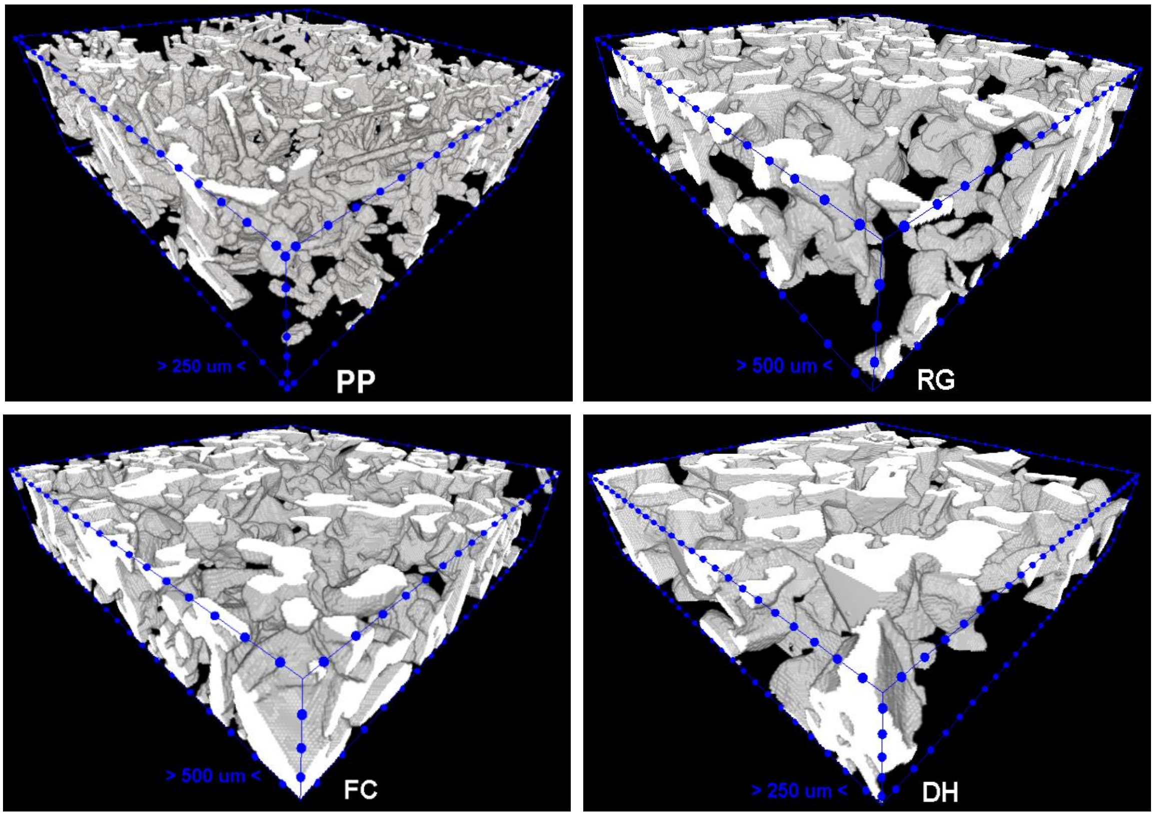

Figure 1: Reconstructed 3D microstructure of representative snow classes; PP (Sample M2), RG (sample S2), FC (sample KFC2) and DH (sample HF5).

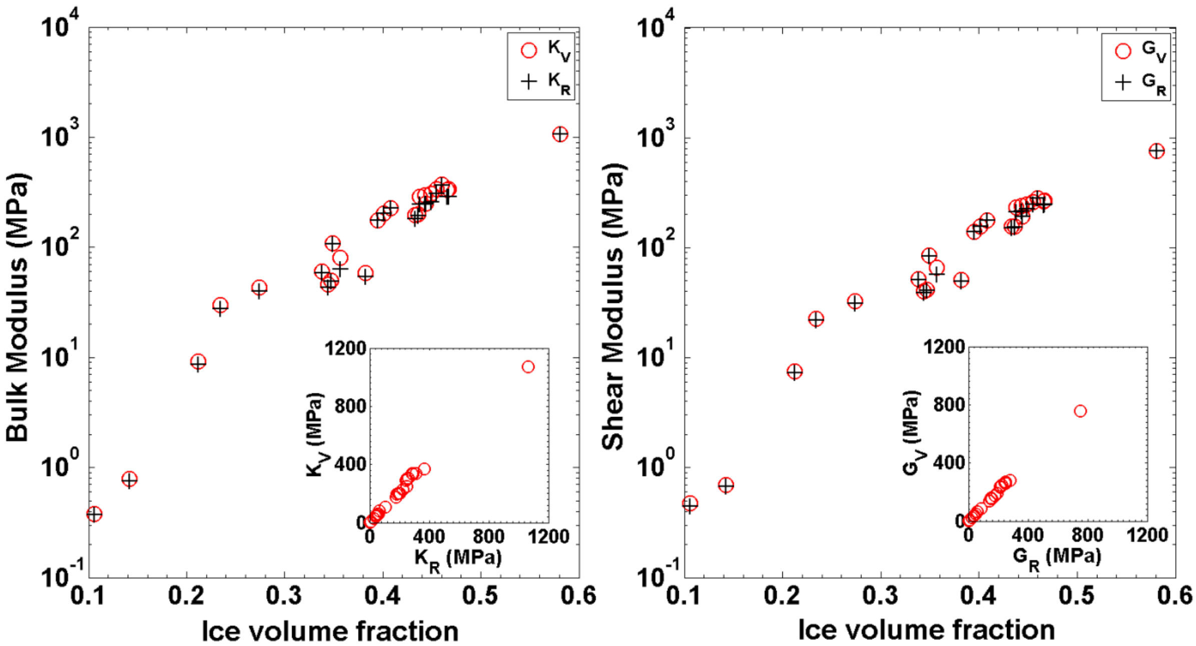

Figure 2: Voigt and Reuss bounds on effective isotropic bulk (k_{eff}) and shear (G_{eff}) modulus computed on the full image volumes for all the samples

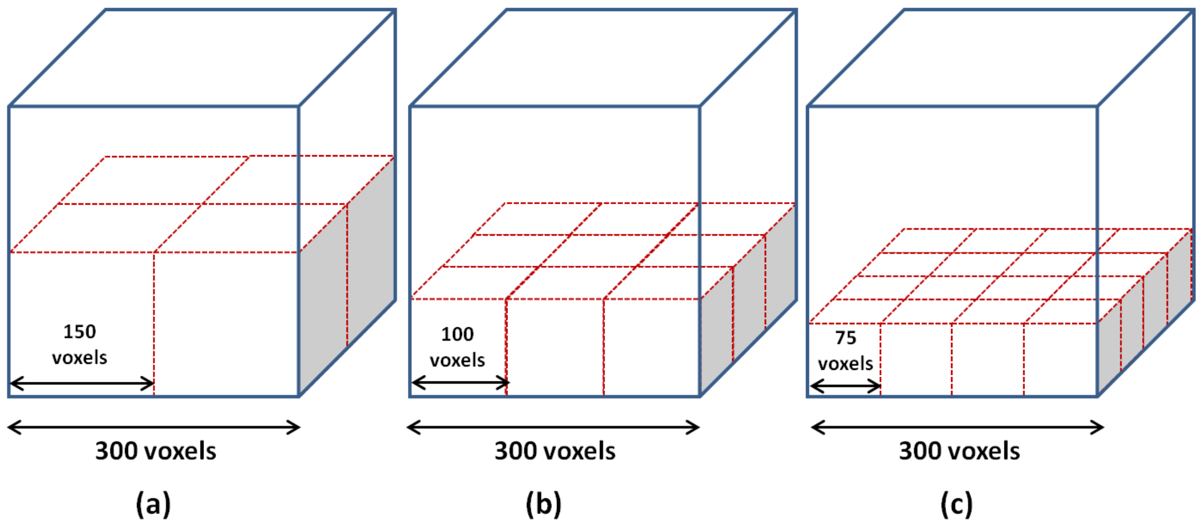

Figure 3: Partitioning procedure to generate three sets of cubical sub-volumes of different edge lengths (L) for investigating the statistical variability. **(a)** set of 8 cubes with L=150 voxels, **(b)** set of 27 cubes with L=100 voxels, and **(c)** set of 64 cubes with L=75 voxels.

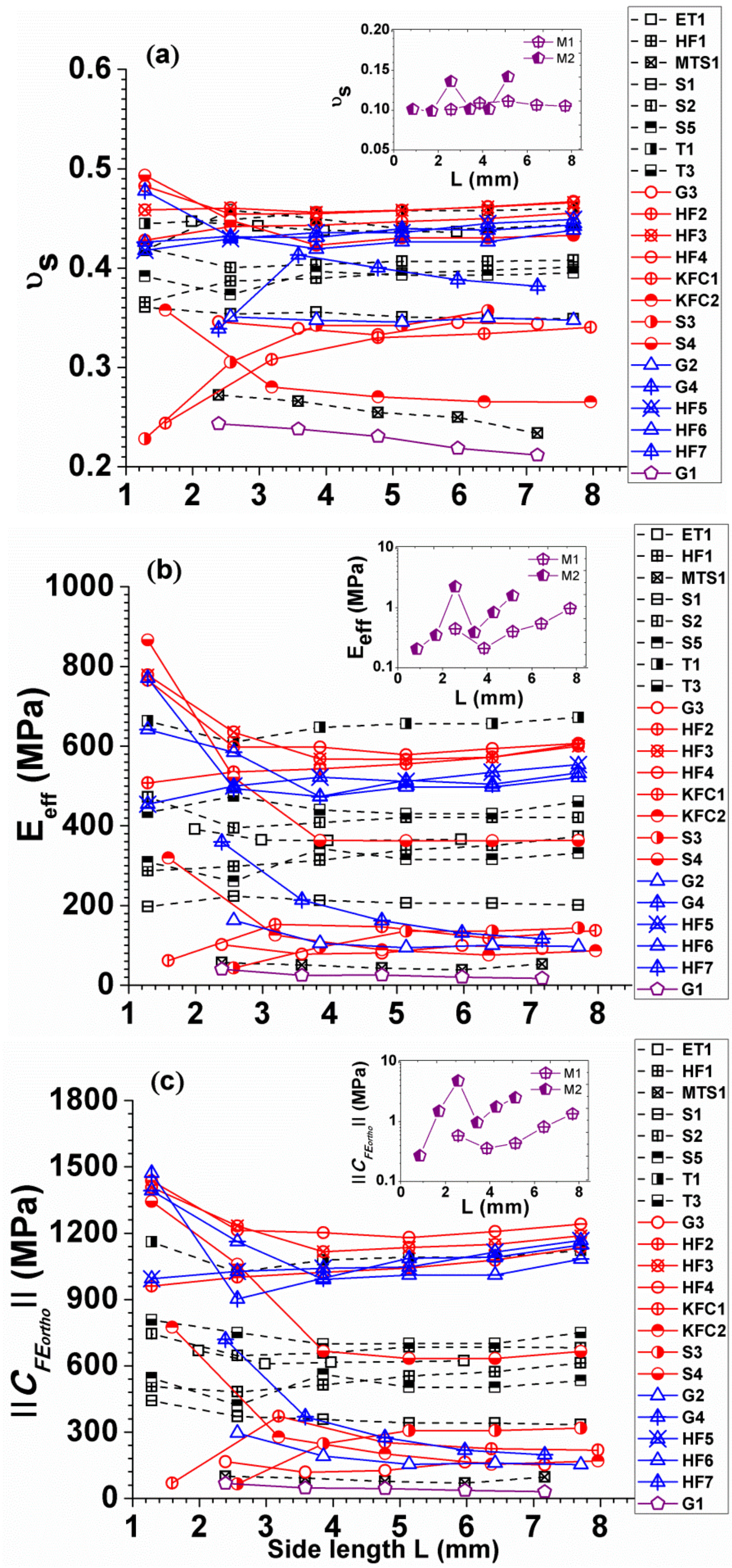

Figure 4: Plots showing convergence of **(a)** ice volume fraction (υ_s), **(b)** Effective Young's modulus (E_{eff}), and **(c)** norm of orthotropic stiffness tensor ($\|\boldsymbol{C}_{FE_{ortho}}\|$), computed on concentric cubic snow volumes of increasing sizes.

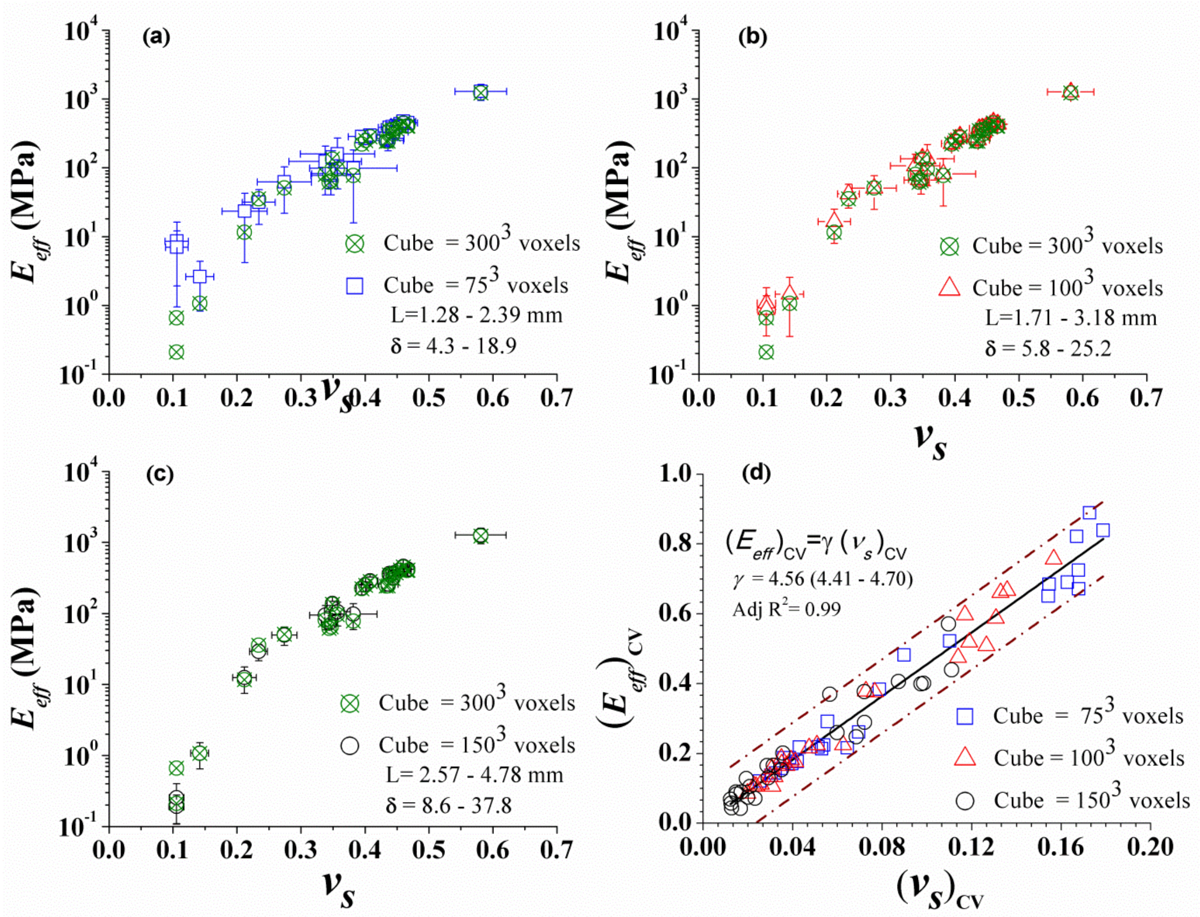

Figure 5: Variation of mean E_{eff} versus mean υ_s for cubical sub-volumes with edge length (L) of **(a)** 75 voxels, **(b)** 100 voxels, and **(c)** 150 voxels. The error bars represent ±one standard deviation. The linear scaling relation showing the correlation between relative variability of a microstructural measure, $(\upsilon_s)_{CV}$, and effective property, $\left(E_{eff}\right)_{CV}$, is shown in **(d)**. Depending on the resolution of individual images, the cube edge lengths of 150 voxel, 100 voxel and 75 voxel translated into physical edge lengths of 2.6-4.8 mm, 1.7-3.2 mm and 1.3-2.4 mm respectively and $\delta := L/l_{micro}$.

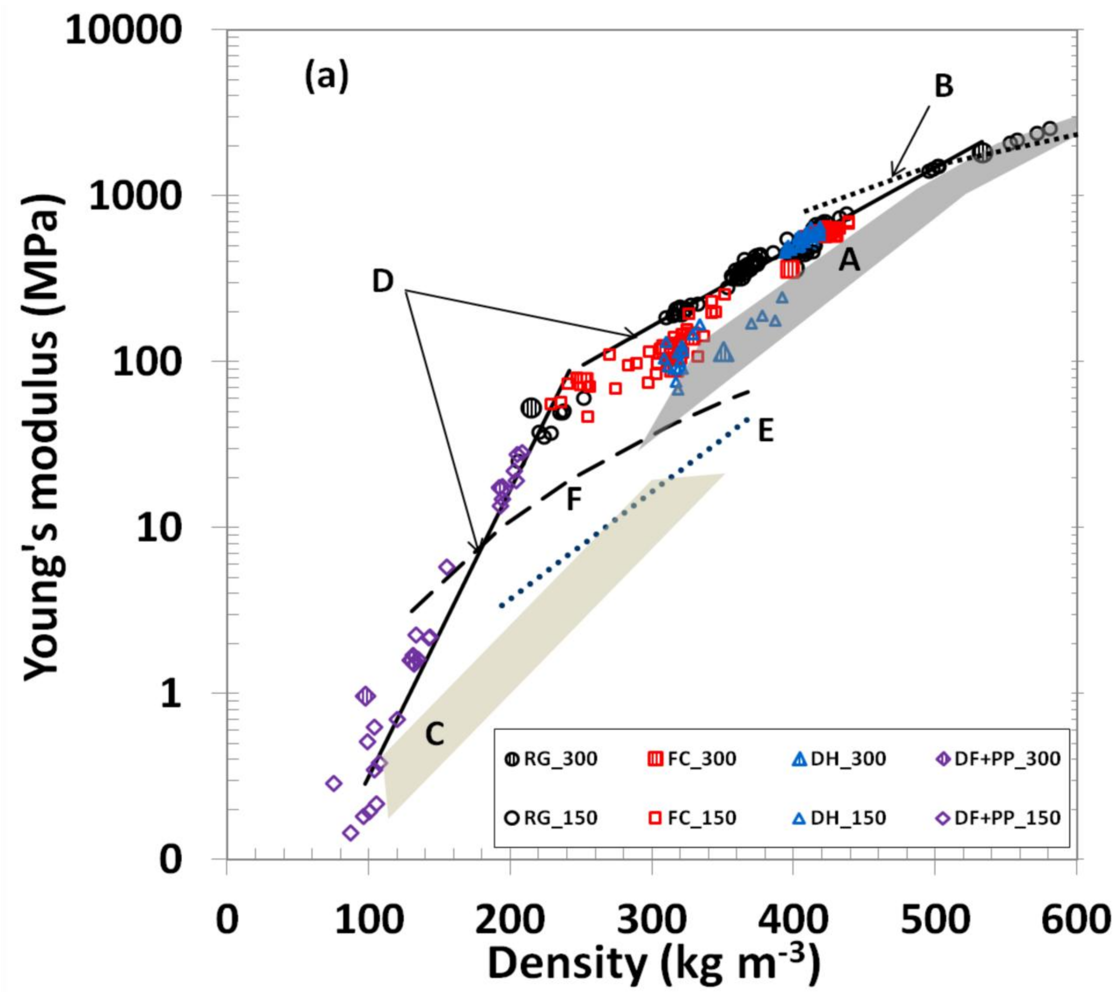

Figure 6: (a) Comparison of E_{eff} with previously published results. Dynamic measurements (A and B) and strain-rate and creep tests results (C) are from Shapiro et al. (1997). μFE simulations based exponential fit (D) from Kochle and Schneebeli, (2014), Laboratory measurements form Scapozza and Bartelt, (2003), (E), and Sigrist et al. (2006), (F), are also included. Open symbols correspond to simulations over sub-volumes with edge length, L=150 voxels, while filled symbols represents results from the full image volume, i.e. L=300 voxels.

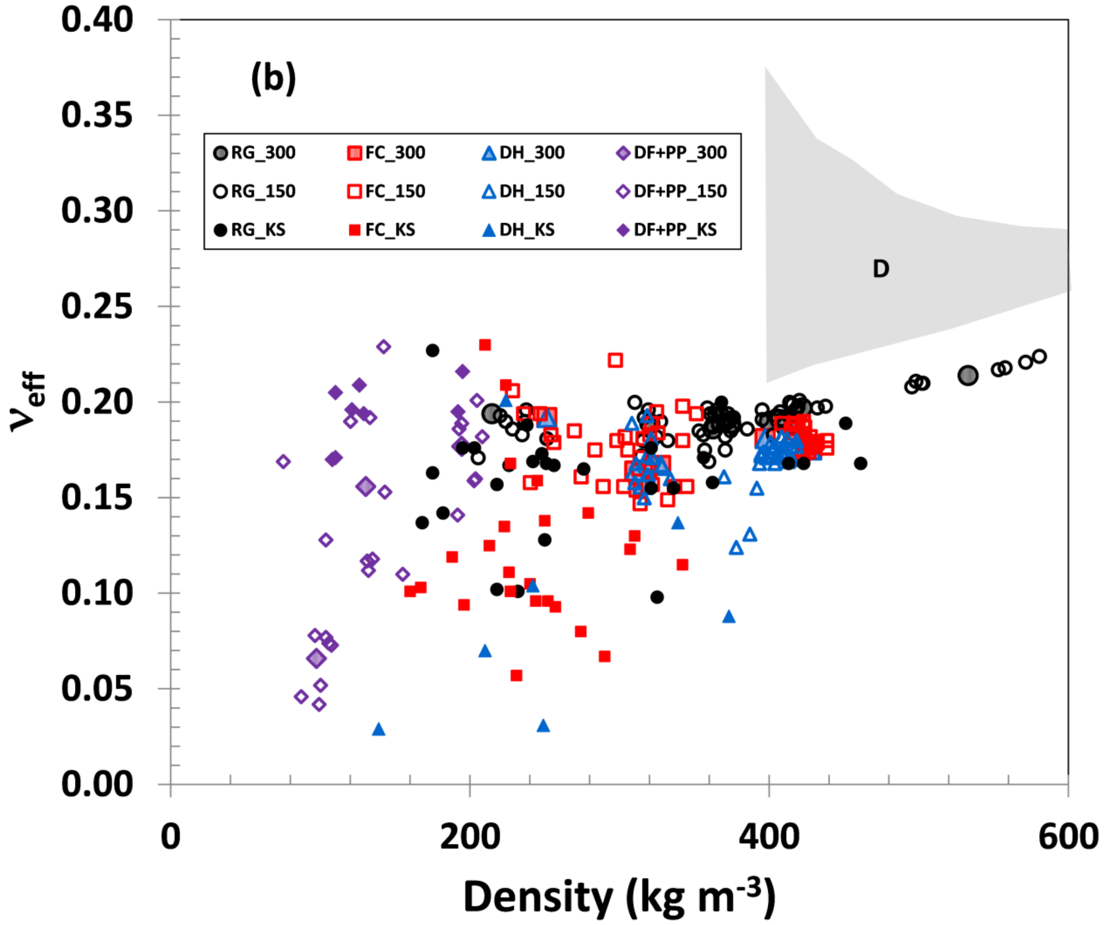

Figure 6: (b) Scatter plot of ν_{eff} with density. Open symbols correspond to simulations over sub-volumes with edge length, L=150 voxels, while light filled symbols represents results from the full image volume, i.e. L=300 voxels. For comparison, μFE results (dark filled symbols) from Kochle and Schneebeli (2014) and measurements (region D) from Smith (1969) are also included.

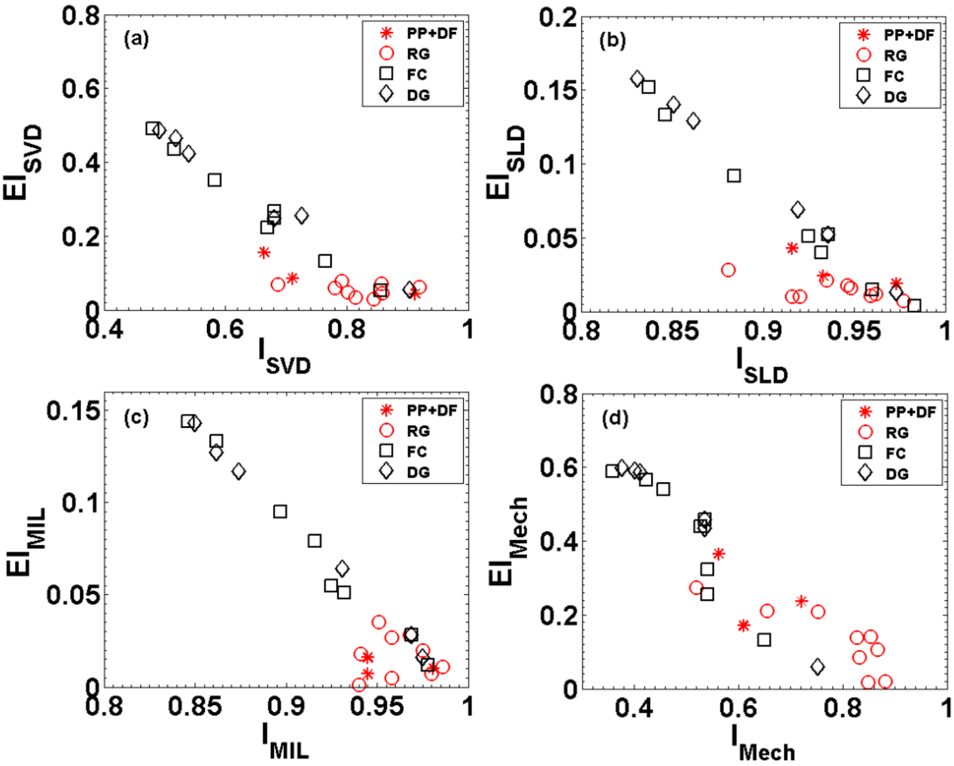

Figure 7: Bivariate plots of elongation index (EI) vs. isotropic index (I) for (a) SVD, (b) SLD and (c) MIL fabric tensors respectively. The corresponding plot between mechanical elongation (EI_{Mech}) and isotropy (I_{Mech}) indices is shown in (d).

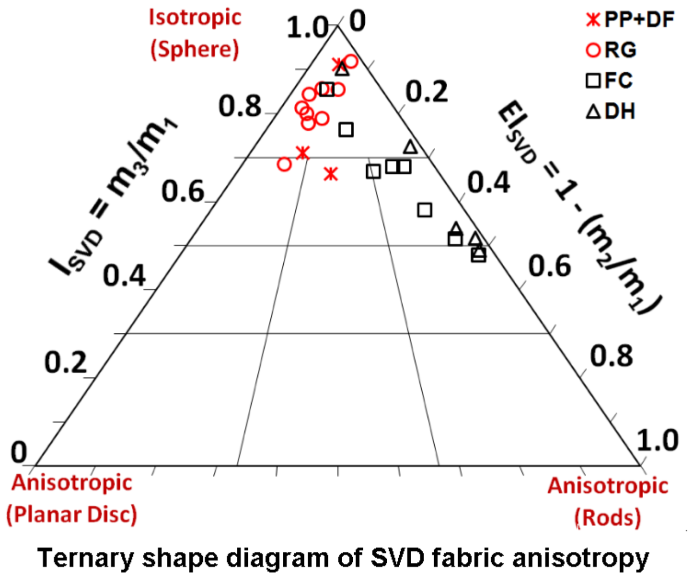

Figure 8: Ternary shape diagram of isotropy and elongation indices derived from SVD fabric measures.

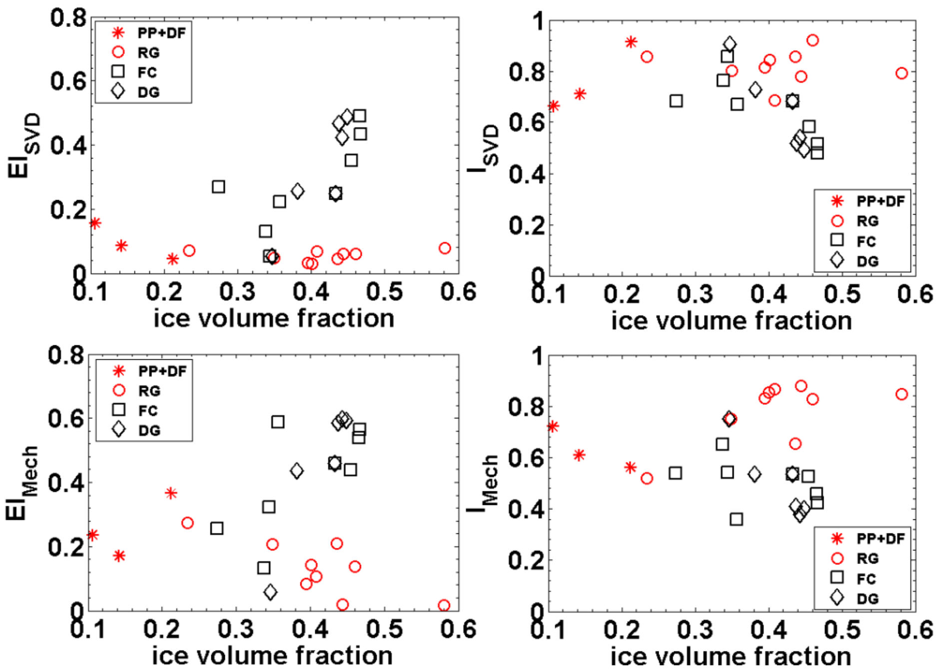

Figure 9: Fabric and mechanical anisotropy indices v/s ice volume fraction

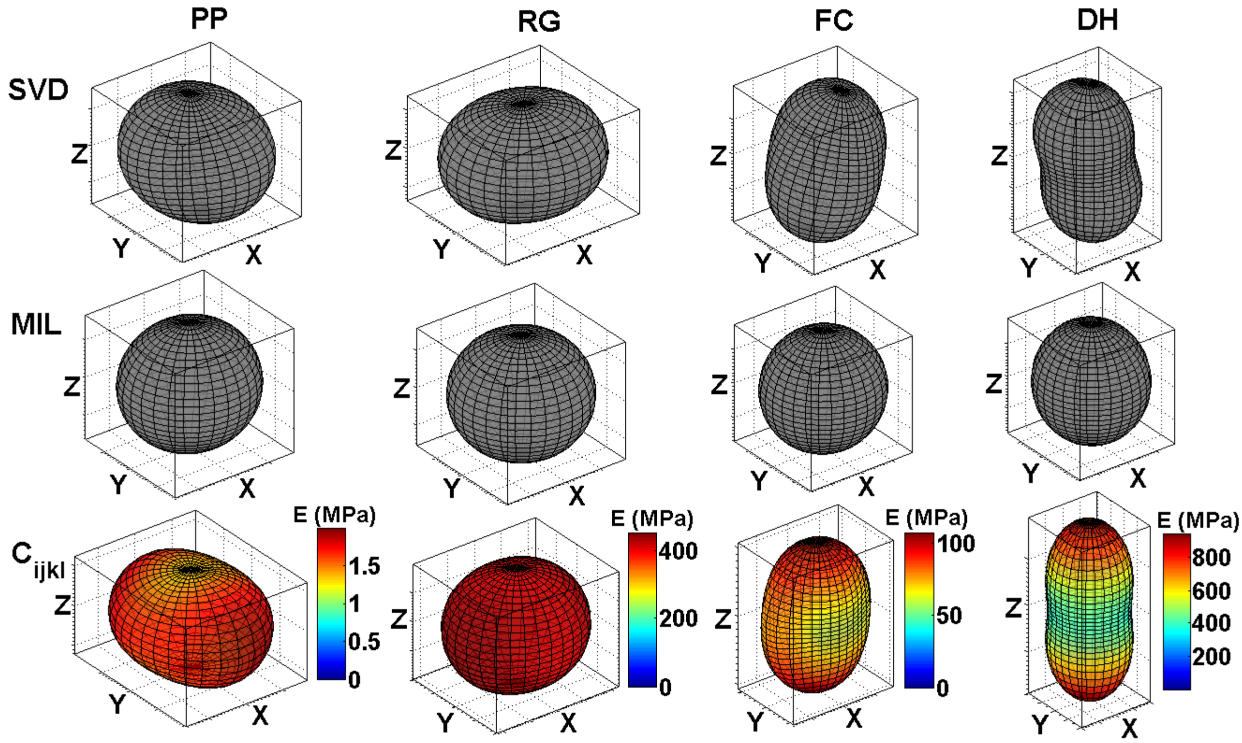

Figure 10: Fabric tensor and orthotropic stiffness tensor ($\boldsymbol{C}_{ijkl}$) representations of snow samples depicted in Figure 1. The top and middle row depicts fabric ellipsoids for SVD and MIL fabric tensors while the bottom row shows the geometrical representations of $\boldsymbol{C}_{ijkl}$ for PP, RG, FC and DH snow classes. The fabric tensors are shown in the original image coordinate system which matches closely with the mechanical main directions obtained via the optimization procedure.

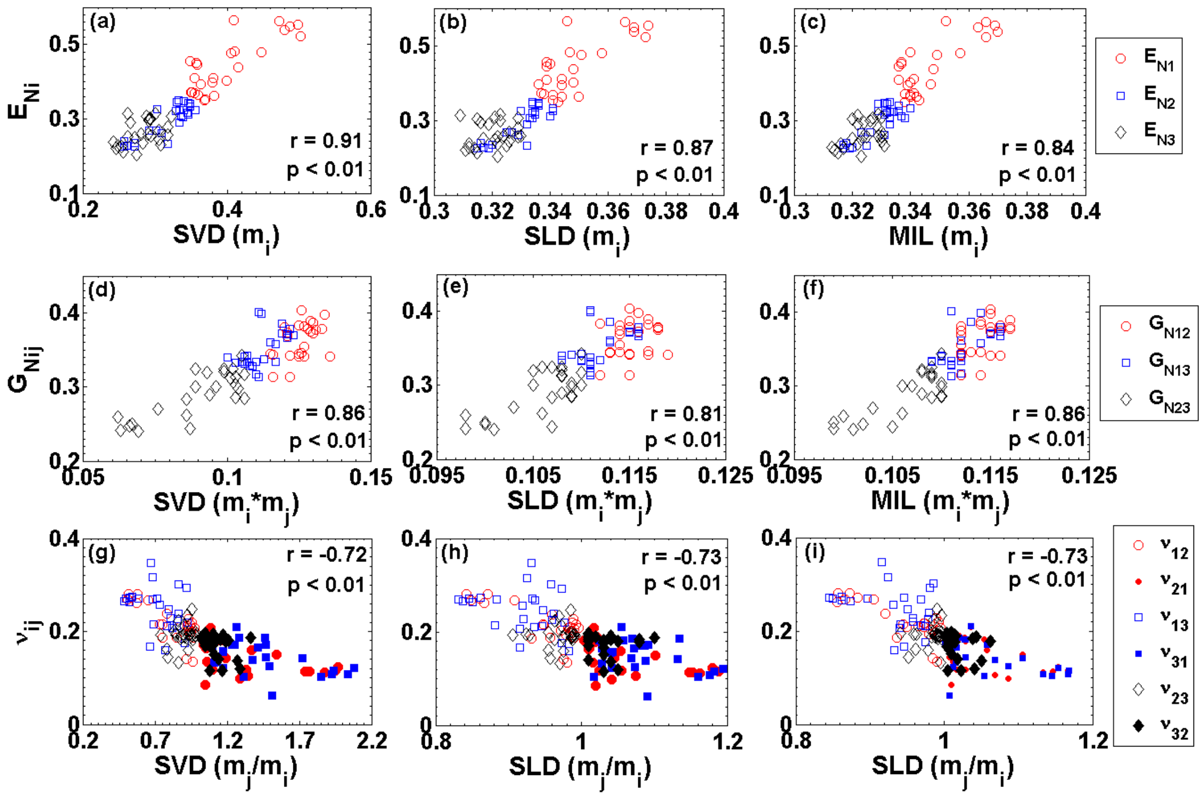

Figure 11: Correlation between normalized orthotropic technical constants (E_{Ni}, G_{Nij}, ν_{ij}) and functions of eigenvalues (m_i) corresponding to MIL, SLD and SVD fabric measures.

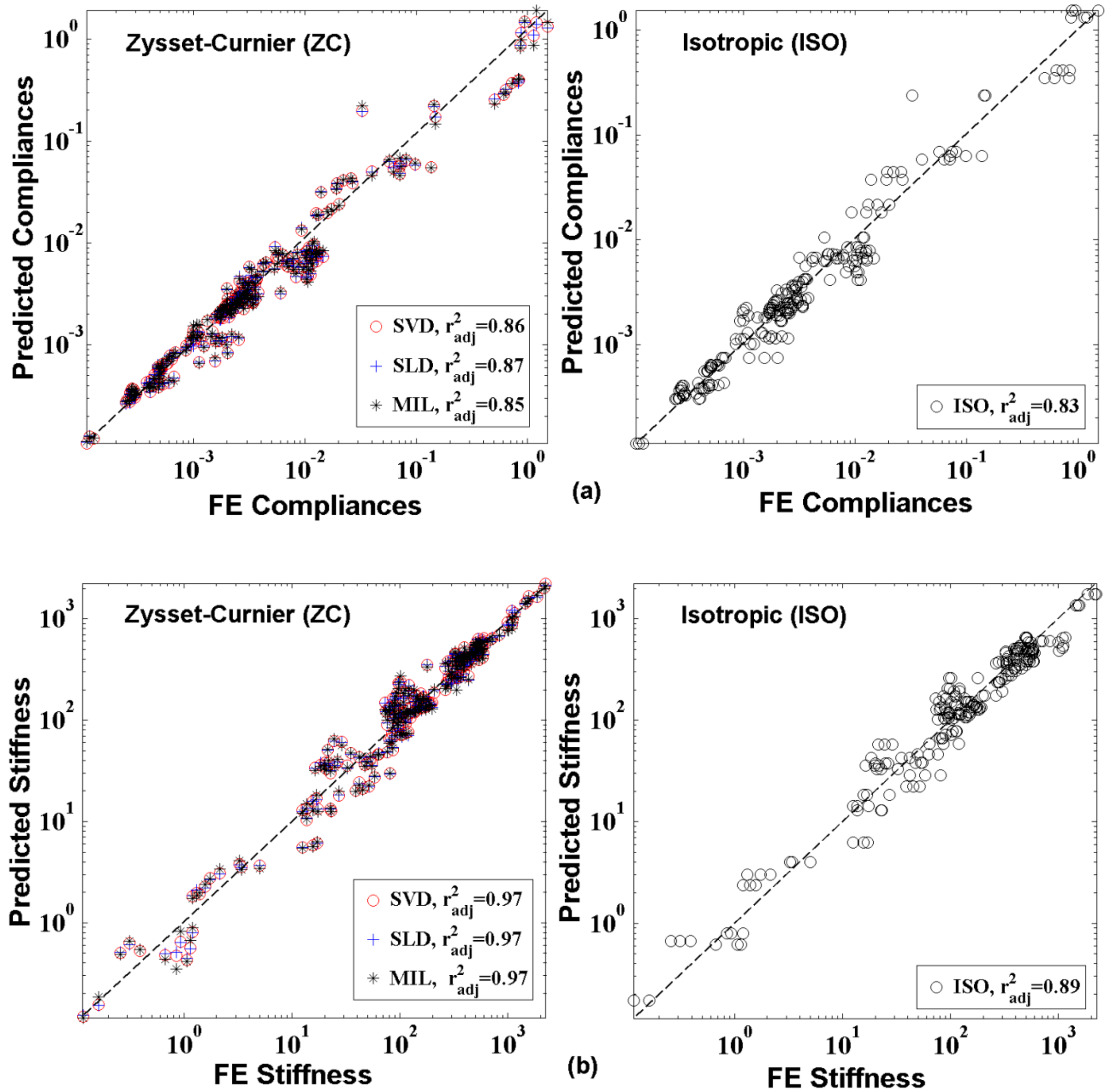

Figure 12: Correlation between μFE computed and predicted components of **(a)** compliance, and **(b)** stiffness tensors using the (i) Zysset-Curnier (ZC) model with SVD, SLD and MIL fabric measures, and (ii) isotropic model.

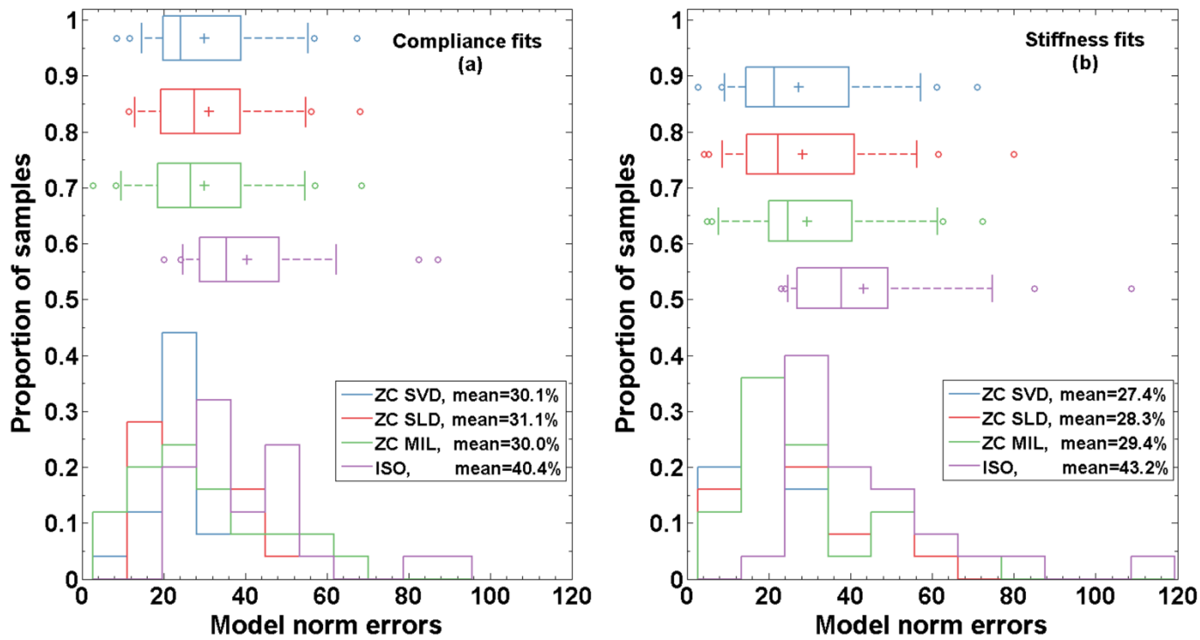

Figure 13: Histograms of model norm errors for **(a)** compliance and **(b)** stiffness approaches. Compared to ISO model, the ZC model produced 24-36% lower relative model norm errors.

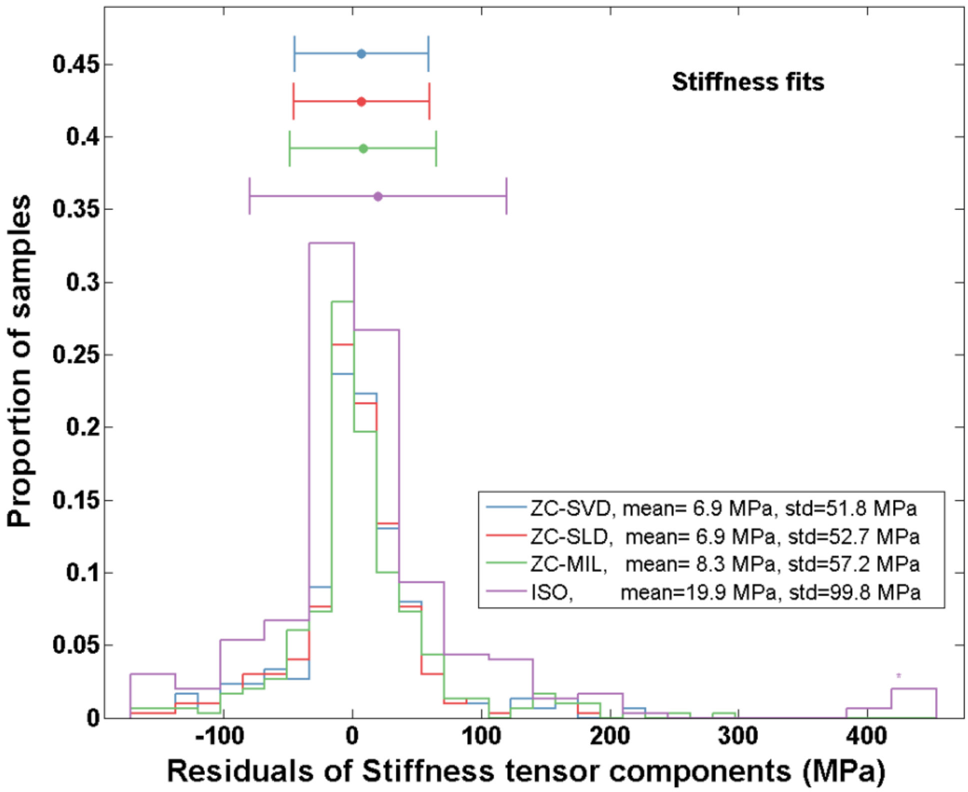

Figure 14: Histograms of residuals of stiffness tensor components for ZC model with SVD, SLD and MIL fabric measures and Isotropic model. Residuals are approximately normally distributed. ZC model appears to perform better with lower mean values and standard deviation of the residuals.

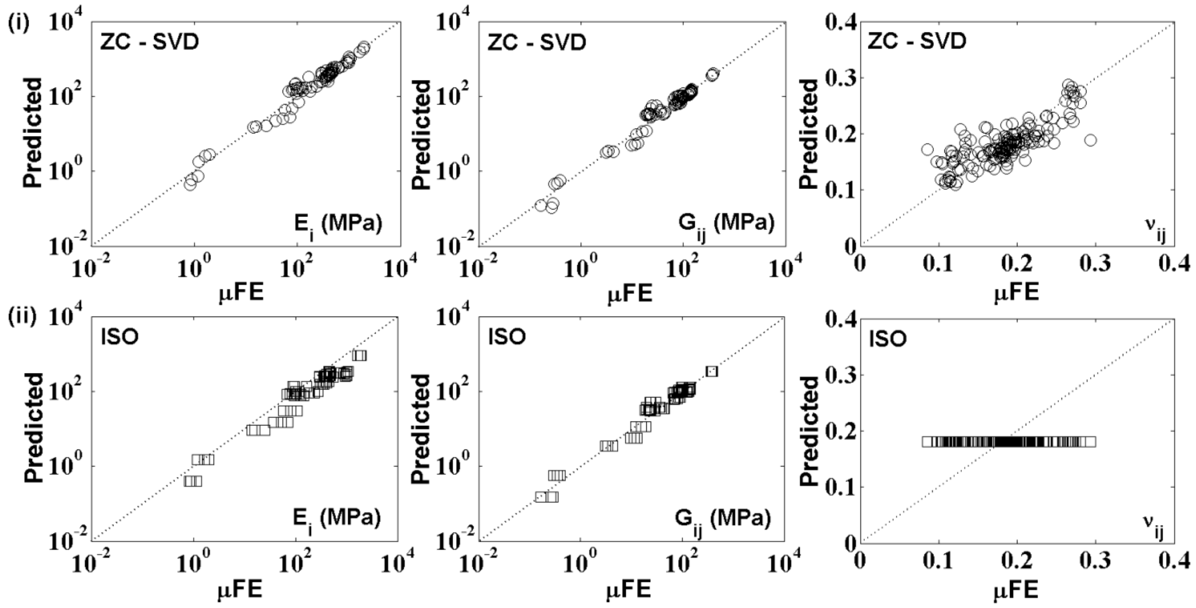

Figure 15: Comparison between μFE computed and predicted engineering constants (E_i, G_{ij}, ν_{ij}) using (i) ZC model with SVD fabric tensor (top row) and, (ii) isotropic model (bottom row).

Highlights:

Micro-FE computation of homogenized anisotropic stiffness and compliance tensor of snow from 3D X-ray tomography images.

Characterization of microstructural anisotropy via volume- and surface based fabric tensors.

Established fabric-elasticity relations for snow based on orthotropic and isotropic models.

Graphical Abstract (for review) -Revised